

Probing type Ia supernova properties using bolometric light curves from the Carnegie Supernova Project and the CfA Supernova Group

R. A. Scalzo^{1,2,3*}, E. Parent^{4,5}, C. Burns⁴, M. Childress^{1,3}, B. E. Tucker^{1,3,6},
 P. J. Brown⁷, C. Contreras⁸, E. Hsiao⁸, K. Krisciunas⁷, N. Morrell⁸, M. M. Phillips⁸,
 A. L. Piro⁸, M. Stritzinger⁹, and N. Suntzeff⁷

¹ *Research School of Astronomy and Astrophysics, Australian National University, Canberra, ACT 2611, Australia*

² *Centre for Translational Data Science, University of Sydney, Darlington, NSW 2008, Australia*

³ *ARC Centre of Excellence for All-Sky Astrophysics (CAASTRO)*

⁴ *Observatories of the Carnegie Institution for Science, Pasadena, CA 91101, USA*

⁵ *Department of Physics and McGill Space Institute, McGill University, Montréal, QC Canada H3A 2T8, Canada*

⁶ *Department of Astronomy, University of California, Berkeley, B-20 Hearst Field Annex #3411, Berkeley, CA 94720-3411, USA*

⁷ *George P. and Cynthia Woods Mitchell Institute for Fundamental Physics and Astronomy, Department of Physics and Astronomy, Texas A&M University, 4242 TAMU, College Station, TX 77843, USA*

⁸ *Carnegie Observatories, Las Campanas Observatory, La Serena, Chile*

⁹ *Department of Physics and Astronomy, Aarhus University, Ny Munkegade 120, DK-8000 Aarhus C, Denmark*

1 March 2022

ABSTRACT

We present bolometric light curves constructed from multi-wavelength photometry of Type Ia supernovae (SNe Ia) from the Carnegie Supernova Project and the CfA Supernova Group, using near-infrared observations to provide robust constraints on host galaxy dust extinction. This set of light curves form a well-measured reference set for comparison with theoretical models. Ejected mass and synthesized ^{56}Ni mass are inferred for each SN Ia from its bolometric light curve using a semi-analytic Bayesian light curve model, and fitting formulae provided in terms of light curve width parameters from the SALT2 and SNOOPY light curve fitters. A weak bolometric width-luminosity relation is confirmed, along with a correlation between ejected mass and the bolometric light curve width. SNe Ia likely to have sub-Chandrasekhar ejected masses belong preferentially to the broad-line and cool-photosphere spectroscopic subtypes, and have higher photospheric velocities and populate older, higher-mass host galaxies than SNe Ia consistent with Chandrasekhar-mass explosions. Two peculiar events, SN 2006bt and SN 2006ot, have normal peak luminosities but appear to have super-Chandrasekhar ejected masses.

Key words: white dwarfs; supernovae: general; cosmology: dark energy; methods: statistical

1 INTRODUCTION

Type Ia supernovae (SNe Ia), the thermonuclear explosions of white dwarfs, were used as extragalactic distance indicators in the discovery of the Universe’s accelerating expansion (Riess et al. 1998; Perlmutter et al. 1999). They play a leading role in ongoing studies aimed at measuring the Hubble constant and the nature of dark energy, and are also a critical component to the chemical enrichment of galaxies over cosmic time (Kobayashi & Nomoto 2009). Despite their central role in astrophysics and cosmology, the evolutionary channels leading to the explosion and the final explosion trigger for SNe Ia have not yet been unambiguously identi-

fied; this represents a challenging, long-standing unsolved problem in the field (for in-depth reviews, see: Wang & Han 2012; Hillebrandt et al. 2013; Ruiz-Lapuente 2014).

Accurate distance measurements to SNe Ia depend on empirical relations between SN Ia peak luminosity, light curve width, and color (Phillips 1993; Phillips et al. 1999; Riess, Press & Kirshner 1996; Tripp 1998; Goldhaber et al. 2001; Guy et al. 2007) and, more recently, a correction based on the host galaxy mass (Kelly et al. 2010; Sullivan et al. 2011; Childress et al. 2013a). There are also established relations between SN Ia luminosity and temperature-dependent ratios of spectral features (Nugent et al. 1995; Bongard et al. 2006; Silverman, Kong & Filippenko 2012), themselves correlated with the light curve width. These relations are well-established observationally, and represent strong con-

* Email: rscalzo@mso.anu.edu.au

straints on SN Ia explosion physics which still remain to be fully explained theoretically. Identification of the SN Ia progenitors could drive theoretical searches for new, independent luminosity correlates, decreasing statistical and systematic uncertainties in measurements of the cosmic distance scale and expansion history.

In most scenarios, the explosion is triggered by interaction of the white dwarf with a binary companion, either a non-degenerate star (“single-degenerate”; Whelan & Iben 1973) or another white dwarf (“double-degenerate”; Iben & Tutukov 1984). In the traditional single-degenerate scenario, a carbon-oxygen white dwarf accretes hydrogen from its companion until igniting spontaneously near the Chandrasekhar limiting mass $M_{\text{Ch}} = 1.4 M_{\odot}$; tests of SN Ia progenitor scenarios thus often focus on evidence for circumstellar hydrogen or for accretion processes. Direct searches for surviving companions in SN Ia remnants (Schaefer & Pagnotta 2012) and in pre-explosion imaging (Li et al. 2011) yielded null results. Upper limits on ionizing radiation from nuclear burning of accreted material on the white dwarf’s surface (Gilfanov & Bogdán 2010; Woods & Gilfanov 2013, 2014) constrain accretion rates. Upper limits on circumstellar hydrogen in most SN Ia systems come from non-detections of interaction flux in early light curves (Hayden et al. 2010; Nugent et al. 2011; Bloom et al. 2012; Olling et al. 2015; Shappee et al. 2015); $H\alpha$ in late-time spectra (Mattila et al. 2005; Leonard 2007; Shappee et al. 2013); radio emission (Panagia et al. 2006; Chomiuk et al. 2012, 2016); and X-ray emission (Margutti et al. 2014). However, these limits strictly rule out only symbiotic nova systems with red giant companion stars. The peculiar “Ia-CSM” (Silverman et al. 2013) subclass shows significant circumstellar interaction luminosity and narrow $H\alpha$ emission (Hamuy et al. 2003; Wood-Vasey, Wang & Aldering 2004; Aldering et al. 2006; Prieto et al. 2007; Dilday et al. 2012; Taddia et al. 2012), but this subclass comprises at most a few percent of all SNe Ia. Cao et al. (2015), Marion et al. (2016), and Hosseinzadeh et al. (2017) present evidence for signatures of single-degenerate companions in the near-ultraviolet and optical light curves of otherwise normal SNe Ia, starting within the first day after explosion but see (but see Shappee et al. 2018, for conflicting evidence in one case). Jiang et al. (2017) report photometric and spectroscopic signatures of *helium* accretion onto the white dwarf that produced the well-observed SN Ia MUSE1604D. Nucleosynthetic constraints, sensitive to the central density of the exploding white dwarf, may also present evidence for or against particular progenitor scenarios (e.g. Seitenzahl et al. 2013a; McWilliam et al. 2017; Shappee et al. 2017).

Another approach is to compare observations to detailed computational models of SN Ia explosions (Röpke et al. 2012; Blondin et al. 2012, 2013; Diemer et al. 2013; Blondin et al. 2017; Hoefflich et al. 2017; Goldstein & Kasen 2018). These comparisons typically focus on tell-tale spectroscopic features or light curves in specific passbands, and/or the distribution of ^{56}Ni in the ejecta. However, the radiation transfer problem for SN Ia atmospheres remains extremely challenging, and any practical solution will approximate some aspects of the physics. Full reproduction of the spectrum, including velocities, strengths, and detailed shapes of atomic line features, is the most stringent possible end-to-end test of an explosion model (Dessart et al. 2014a,b). It can be difficult to determine whether discrepancies with observations represent failures of the underlying scenario or merely some aspect of the calculation. Single strong spectroscopic features with uncertain behavior, such as the Ca II infrared triplet (Kasen 2006), may also have dramatic influence on single-band light curves.

In contrast, the *bolometric* light curve — the total radiant energy output from the SN Ia as a function of time — is easier to

simulate numerically (e.g. Wygoda, Elbaz & Katz 2017; Sukhbold 2018) and can even be predicted semi-analytically (Arnett 1982; Pinto & Eastman 2000a,b), but requires high-quality data with broad wavelength and high-cadence temporal coverage to measure observationally. The bolometric light curve is sensitive to fundamental physical parameters of the explosion, including the mass M_{Ni} of radioactive ^{56}Ni synthesized (which powers the light curve via the decay chain $^{56}\text{Ni} \rightarrow ^{56}\text{Co} \rightarrow ^{56}\text{Fe}$) and the total ejected mass M_{ej} . These global parameters provide a complementary probe of the different explosion mechanisms currently being tested. The traditional single-degenerate scenario implies $M_{\text{ej}} = M_{\text{Ch}}$, but other mechanisms with different progenitor masses could produce events resembling SNe Ia: explosions of rapidly rotating, super-Chandrasekhar-mass white dwarfs partially supported by accreted angular momentum (Justham 2011; Di Stefano & Kilic 2012); super-Chandrasekhar-mass mergers of two white dwarfs (e.g. Pakmor et al. 2011, 2012); “tamped detonations” resulting from relaxed white dwarf merger products surrounded by a thick carbon-oxygen envelope (Khokhlov, Mueller & Hoefflich 1993; Hoefflich & Khokhlov 1996); *helium* detonations on a sub-Chandrasekhar-mass white dwarf’s surface (Woosley & Weaver 1994; Sim et al. 2010; Fink et al. 2010); and collisions of two white dwarfs (Rosswog et al. 2009; Raskin et al. 2010; Thompson 2011; Kushnir et al. 2013). Some authors have even looked into mechanisms enabling the spontaneous explosion of isolated white dwarfs (Chiosi et al. 2015; Bramante 2015).

Full bolometric light curves have been built for a relatively small sample of normal SNe Ia (Suntzeff 1996; Vacca & Leibundgut 1996; Contardo, Leibundgut & Vacca 2000; Stritzinger et al. 2006; Scalzo et al. 2014a). However, the available light curves have had a significant impact on development of SN Ia theory. Stritzinger et al. (2006) used semi-analytic modeling of 16 SN Ia bolometric light curves to infer a range of ejected masses from 0.5–1.4 M_{\odot} , which spurred important advances into sub-Chandrasekhar-mass explosion models (Fink et al. 2010; Kromer et al. 2010; Sim et al. 2010). Scalzo et al. (2014a) used an improved version of the technique on 19 additional SNe Ia in the nearby Hubble flow, finding evidence that most normal SNe Ia have $M_{\text{ej}} = 1.0\text{--}1.4 M_{\odot}$, and that M_{ej} correlates strongly with light curve width parameters used in cosmology (Scalzo et al. 2014a). Scalzo, Ruiter & Sim (2014) used this correlation as a starting point to reconstruct the intrinsic distribution of M_{ej} from a much larger sample of SNe Ia; they found that a significant fraction (at least 25%) of all normal SNe Ia must explode beneath the Chandrasekhar limiting mass for white dwarfs, and that the joint $M_{\text{ej}}\text{--}M_{\text{Ni}}$ distribution could not be explained by any single contemporary explosion scenario. Subsequent theoretical work supports connections between the mass distribution of SNe Ia and the width-luminosity relation (Wygoda, Elbaz & Katz 2017; Blondin et al. 2017; Blondin, Dessart & Hillier 2018; Goldstein & Kasen 2018).

This work presents a set of high-quality bolometric light curves constructed with public data from the *Carnegie Supernova Project* (CSP-I; Hamuy et al. 2006) and the Harvard-Smithsonian Center for Astrophysics Supernova Group (CfA). Sample selection is described in §2, host galaxy reddening in §3, and the procedure for constructing bolometric light curves from multi-band data in §4. A semianalytic modeling suite (§5) developed in previous papers (Scalzo et al. 2010, 2012, 2014a,b) is used to infer ^{56}Ni masses and ejected masses from the bolometric light curves. Correlations between these global explosion parameters and other observables such as spectroscopic subtype or host galaxy mass are presented in §6. Implications for the width-luminosity relation, the physics

of peculiar SNe Ia, and related questions are examined in §7, and conclusions and prospects for future work set out in §8.

2 OBSERVATIONS AND SAMPLE SELECTION

The SNe Ia we use for our investigation are drawn from the multi-year CSP-I and CfA data sets. These surveys followed targets from searches that target known nearby galaxies, unlike the untargeted search and follow-up program by the Nearby Supernova Factory that discovered most of the SNe Ia analyzed in Scalzo et al. (2014a). Peculiar events are over-represented since they are strongly selected for follow-up observations; they will be brighter and easier to observe if they are overluminous, and will be observed more aggressively than normal SNe Ia if they are subluminous. The current sample is thus useful for exploring the diversity of SN Ia bolometric light curve behavior.

We use CSP-I $uBVgri$ photometry from Stritzinger et al. (2011), and CfA $UBVRi'r'i'$ photometry from Jha, Riess & Kirshner (2007), Hicken et al. (2009), and Hicken et al. (2012). Near-infrared (NIR) photometry is also available from Stritzinger et al. (2011) for CSP-I targets, and from Friedman et al. (2015) for CfA targets. We use all photometry in each group’s natural system, based on the transmission functions published in the source papers.

We use derived spectroscopic quantities published in Blondin et al. (2012), Silverman, Kong & Filippenko (2012), and Folatelli et al. (2013), including:

- (i) the heliocentric and CMB-frame redshifts of the host galaxy;
- (ii) the blueshift velocity v_{Si} of the Si II $\lambda 6355$ feature in spectra near maximum light;
- (iii) the spectroscopic subtype identified by SNID (Blondin & Tonry 2007):
- (iv) the Wang et al. (2009) subtype — “normal” (N) or “high-velocity” (HV) — determined by whether v_{Si} is greater or less than $11,800 \text{ km s}^{-1}$;
- (v) the Branch et al. (2006) subtype, based on measurements of the equivalent widths and line profile shapes of the Si II $\lambda 5972$ and Si II $\lambda 6355$ features in spectra taken near maximum light.

Some SNe Ia in our sample have host galaxy stellar masses available from previous literature analyses. Twenty-two targets have host masses from Neill et al. (2009), who employ common-aperture photometry on multi-wavelength data for the host galaxies of nearby targets. Similarly, Childress et al. (2013b) derive host masses with common aperture photometry for the sample of SNe Ia observed by the Nearby Supernova Factory; 4 SNe Ia from our sample have published host galaxy masses from this work. Finally, 2 SNe Ia from our sample have host masses from Kelly et al. (2010). All of these analyses have comparable mass values (i.e. compatible initial mass functions). We adopt errors on host mass values as the quadrature sum of the published mass errors (from measurement errors) and a 0.15 dex systematic error term which Childress et al. (2013b) found to be an appropriate assessment of the systematic uncertainty on galaxy mass-to-light ratios arising from variations in star-formation histories.

The degree of temporal and wavelength completeness required for building broad-band bolometric light curves means that even some of the best-observed objects may be missing data in observationally demanding bandpasses such as NIR. To minimize the impact of corrections for missing flux, we apply strict selection criteria described below, starting from a total of 358 targets (85 from CSP-I and 324 from CfA, with 34 observed by both programs).

An accurate measurement of a SN Ia’s luminosity requires an accurate distance measurement, which can be ensured by restricting the sample to the smooth Hubble flow, since direct distance measurements are in general not available for very nearby targets. However, most of the CSP-I and CfA SNe Ia were discovered by searches targeting specific nearby galaxies, and closer SNe Ia will in general have higher-quality, more complete data. To avoid too strict a selection, we choose targets with $z > 0.013$ (4000 km s^{-1}). Assuming a random peculiar velocity of 300 km s^{-1} for each SN Ia host galaxy (Davis et al. 2011), the induced systematic error on the peak luminosity of each SN Ia, and hence the ^{56}Ni mass derived from the light curve, will be less than 15% — about the limit of accuracy that can be achieved with the inference methods of Scalzo et al. (2014a) with the best available data. This cut removes 16 CSP-I targets and 62 CfA targets.

To capture as much of the SN Ia radiation as possible at each observation epoch, and to adequately sample the shape of the bolometric light curve, we require each target to have the equivalent of full wavelength coverage from $4000\text{--}9000 \text{ \AA}$ ($BVRI$ equivalent) for at least one time point from each of a set of key light curve phases, defined with respect to the date of B -band maximum light as defined by the “color model” of the SNOOPY light curve fitter (Burns et al. 2011, 2014):

- (i) between days -8 and $+0$ (BV bands only), to ensure a robust constraint on the light curve width and host galaxy reddening;
- (ii) within 3 days of day -1 (bolometric maximum; Scalzo et al. 2014a), to ensure a robust constraint on the ^{56}Ni mass;
- (iii) within 3 days of day $+14$, to ensure that the decline of the bolometric light curve is well-constrained;
- (iv) between day $+21$ and day $+35$, to ensure a robust constraint on the evolution of the spectral energy distribution (SED) between photospheric and early nebular phase; and
- (v) between day $+40$ and day $+80$, to constrain the late-time light curve and the ejected mass.

Our best targets will also have $3300\text{--}4000 \text{ \AA}$ (U or u equivalent) at all of these epochs, enabling measurement of the full $UBVRI$ flux. Other targets have good U/u coverage near maximum light, but with deteriorating signal-to-noise post-maximum, as line blanketing from developing Fe II features redistributes flux from blue wavelengths to the NIR. The requirement of U -band or u -band coverage at more than three weeks past maximum light is thus restrictive, in tension with a required minimum redshift for our targets. The U/u light curves vary significantly between individual SNe Ia, but the CSP-I $u - g$ and CfA $U - B$ colors evolve slowly after day $+20$, and the contribution to the bolometric flux could be adequately modeled by a template at these late phases. We therefore require U/u data only out to day $+20$.

The phase coverage requirements eliminate 40 CSP-I targets and 249 CfA targets. We are left with 39 unique SNe Ia: 29 with CSP-I data, 13 with CfA data, and 3 (SN 2005eq, SN 2005hc, and SN 2006ax) with light curves from both programs that pass all of our selection criteria. Of these, 27 targets have U/u coverage out past day $+40$.

Our sample includes the spectroscopic subtype exemplar SN 1999aa, the slow-declining SN 2004gu, and the 1991bg-like SN 2006gt and SN 2007ba. It also includes the CfA light curve of the peculiar SN Ia 2006bt (Foley et al. 2010). To examine this interesting target in more detail, we also include the CSP-I light curves of SN 2006bt and the similar event SN 2006ot (from Stritzinger et al. 2011), which have excellent temporal and wavelength coverage across the region critical for our analysis but do not pass all of our formal selection criteria. We consider in detail the impact of missing data and photometric peculiarity in our analysis

of these events. Finally, we include the CfA light curve of the over-luminous “super-Chandra” SN 2006gz (Hicken et al. 2007), which has never undergone this type of detailed bolometric light curve analysis despite its importance in characterizing the observational properties of this subclass. SN 2006gz lacks full wavelength coverage around day +14, but this will not affect our inference of explosion properties.

Whenever possible, we have used NIR photometry to improve constraints on the reddening $E(B - V)_{\text{host}}$ and the extinction law slope $R_{V,\text{host}}$ due to dust in the host galaxy. The NIR behavior is quite regular, with its contribution to the luminosity ranging from 6% near B -band maximum light to nearly 30% a few weeks later, and can be well-modeled by a template (Scalzo et al. 2014a). Most of our targets have at least some NIR data near maximum light. Nine targets also have good phase coverage in CSP YJH , resulting in full wavelength coverage from 3300–17500 Å for each of our critical light curve phases. Only the older CfA targets from Jha, Riess & Kirshner (2007) lack NIR data entirely, resulting in greater uncertainties on $E(B - V)_{\text{host}}$ and $R_{V,\text{host}}$ which we take into account in our analysis.

Table 1 lists the SNe Ia and light curves that have passed our selection criteria. Light curve fit results from the SALT2 light curve fitter (Guy et al. 2007, 2010), which we include for connection to previous literature and to provide an alternative parametrization of light curve shape for this work, can be found in the Online Supplementary Material.

Unobserved ultraviolet (UV) flux bluewards of 3300 Å can in principle have a dramatic effect on inferences about M_{Ni} (Scalzo et al. 2014b). Photometry in this wavelength range is rarely available for targets with $z > 0.02$, and has been published for only two SNe Ia in our sample, SN 2007S and SN 2008hv. To correct for this missing flux, we construct a template using published photometry from a separate sample of 79 SNe Ia observed with the Ultra-Violet/Optical Telescope (UVOT; Roming et al. 2005) on the *Swift* spacecraft (Gehrels et al. 2004). The UV photometry was obtained from the *Swift* Optical/Ultraviolet Supernova Archive¹ (SOUSA; Brown et al. 2014). The reductions for the light curves are based on that of Brown et al. (2009), including subtraction of the host galaxy count rates, and using the revised UV zeropoints and time-dependent sensitivity from Breeveld et al. (2011). Where available, we also used public optical-wavelength spectra from the Open Supernova Catalog (Guillochon et al. 2017). Further details on the template construction are provided in §S1 below.

3 HOST GALAXY EXTINCTION

To retrieve a reliable bolometric light curve, correction for extinction by dust in the host galaxy is of paramount importance. Rigorous and robust estimation of $E(B - V)_{\text{host}}$ and $R_{V,\text{host}}$ requires measurements spanning a wide range of wavelengths, which fortunately are ensured by our selection criteria.

3.1 Fitting multi-band light curves with SNOOPY

Our estimates for $E(B - V)_{\text{host}}$ and $R_{V,\text{host}}$ come from the hierarchical Bayesian model built into the SNOOPY light curve fitter (Burns et al. 2011, 2014), which samples the full posterior distribution of $E(B - V)_{\text{host}}$ and $R_{V,\text{host}}$ via Markov chain Monte Carlo (MCMC). The Burns et al. (2014) light curve template is

parametrized by a new light curve width parameter, s_{BV} , proportional to the rest-frame time interval Δt_{BV} between B -band maximum light and the date of maximum $B - V$ color of the SN Ia ($s_{BV} = 1$ for $\Delta t_{BV} = 30$ days). This parametrization more accurately captures the morphological differences between the NIR light curves of normal and 1991bg-like events, compared to contemporary light curve parameters like Δm_{15} .

As a Bayesian model, the Burns et al. (2014) extinction model can incorporate prior information about $E(B - V)_{\text{host}}$, $R_{V,\text{host}}$, and correlations between the two. For our work here, we place a “Gaussian bin” prior on $R_{V,\text{host}}$ as a function of $E(B - V)_{\text{host}}$, in which the data are binned by $E(B - V)_{\text{host}}$ and an independent separate Gaussian prior on $R_{V,\text{host}}$ is placed on SNe Ia within each bin (see figure 14 of Burns et al. 2014). Due to a numerical instability in the Fitzpatrick (1999) reddening law at low $R_{V,\text{host}}$, we impose a limit $R_{V,\text{host}} > 0.5$. An improper uniform prior was used for $E(B - V)_{\text{host}}$, so that negative values were possible; during testing, large negative $E(B - V)_{\text{host}}$ was often a sign of poor data quality. Of the SNe Ia selected for our main analysis, only one (SN 2006kf) has a negative mean $E(B - V)_{\text{host}}$ of -0.03 ± 0.02 mag, consistent with zero extinction.

Since SNOOPY was trained on CSP-I data, it can be used directly on CSP-I photometry. For CfA targets, we S -correct the CfA (including PAIRITEL) data to the CSP-I natural system, using the appropriate filter transmission curves and the Hsiao et al. (2007) spectral template.

To estimate systematic errors in the fit parameters introduced by the S -corrections, we select a joint subset of CSP-I and CfA SNe with slightly more permissive selection criteria than for the bolometric light curve analysis, requiring rest-frame $BVRI$ coverage but relaxing the redshift cut and the requirement for any data beyond day +35. This criterion provides a larger comparison sample (15 SNe Ia) while ensuring that coverage is similar to the bolometric light curve sample in the range of phases needed to constrain the multi-band light curve fit parameters. Each SN Ia in this subsample satisfies the light curve quality cuts on both CSP-I and CfA multi-band photometry, so that temporal completeness should not strongly affect results.

Figure 1 shows comparisons of four indicative SNOOPY outputs (s_{BV} , $E(B - V)_{\text{host}}$, $R_{V,\text{host}}$, and B_{max}) using CSP-I data with those obtained from S -corrected CfA data for the same SNe Ia. The correspondence is good, though not without outliers. Using the 68% confidence half-width as a robust dispersion measure gives a core dispersion of 0.03 in s_{BV} and 0.05 mag in $E(B - V)_{\text{host}}$. The outliers tend to lack NIR and/or pre-maximum constraints in the CfA light curve (SN 2006gj, SN 2007ai) or lie at the extremes of s_{BV} (SN 2005ke, SN 2007S). Estimates of $R_{V,\text{host}}$ track each other well and are consistent within the given uncertainties, which can be large for SNe Ia without NIR data or with low values of $E(B - V)_{\text{host}}$.

For purposes of our modeling, this level of accuracy in the light curve fit parameters is adequate. The SNOOPY fit results for the reddening-corrected maximum B magnitude, $m_{B,\text{max}}$, are consistent within the given uncertainties for all CSP-I and CfA light curves, so that our inferences about the peak luminosity and ^{56}Ni mass should be equivalent for the two surveys.

3.2 Comparison with BAYESN

Twenty-nine CfA SNe Ia from our extinction comparison sample (which may not have corresponding CSP-I light curves) have values of $E(B - V)_{\text{host}}$ and $R_{V,\text{host}}$ derived from the BAYESN light curve fitter, applied to CfA data and published in table 4

¹ http://swift.gsfc.nasa.gov/docs/swift/sne/swift_sn.html

Table 1. Basic SN Ia properties and spectroscopic subclass membership

Name	Survey	z_{helio}	z_{CMB}	$E(B - V)_{\text{MW}}$ (mag)	Branch Type	Wang Type	SNID Type	Corr. ^a
SN 1999aa	CfA	0.01438	0.01522	0.040	SS	91T	99aa	NIR
SN 1999dq	CfA	0.01433	0.01356	0.109	SS	91T	99aa	NIR
SN 2000dk	CfA	0.01743	0.01644	0.069	CL	N	norm	NIR
SN 2001V	CfA	0.01502	0.01606	0.020	SS	91T	91T	NIR
SN 2002hu	CfA	0.03900	0.03824	0.045	SS	91T	99aa	NIR
SN 2004ef	CSP-I	0.03100	0.02977	0.056	BL	HV	norm	NIR
SN 2004eo	CSP-I	0.01572	0.01473	0.108	CL	N	norm	NIR
SN 2004ey	CSP-I	0.01580	0.01463	0.139	CN	N	norm	NIR
SN 2004gs	CSP-I	0.02659	0.02750	0.031	CL	N	norm	UV+NIR
SN 2004gu	CSP-I	0.04579	0.04690	0.026	SS	91T	pec	UV+NIR
SN 2005M	CSP-I	0.02196	0.02297	0.031	SS	91T	91T	...
SN 2005al	CSP-I	0.01241	0.01329	0.055	—	—	norm	NIR
SN 2005el	CSP-I	0.01487	0.01489	0.114	CN	N	norm	...
SN 2005eq	CSP-I	0.02895	0.02835	0.074	SS	91T	91T	NIR
SN 2005eq	CfA	0.02895	0.02835	0.074	SS	91T	91T	...
SN 2005hc	CSP-I	0.04593	0.04498	0.033	CN	N	norm	UV+NIR
SN 2005hc	CfA	0.04593	0.04498	0.033	CN	N	norm	UV+NIR
SN 2005hj	CSP-I	0.05800	0.05695	0.039	SS	91T	99aa	UV+NIR
SN 2005iq	CSP-I	0.03405	0.03293	0.022	CN	N	norm	NIR
SN 2005ki	CSP-I	0.01917	0.02037	0.032	CN	N	norm	NIR
SN 2005ls	CfA	0.02114	0.02054	0.093	—	—	norm	UV+NIR
SN 2006S	CfA	0.03210	0.03296	0.017	SS	N	99aa	NIR
SN 2006ac	CfA	0.02309	0.02394	0.016	BL	HV	norm	...
SN 2006ax	CSP-I	0.01671	0.01796	0.050	CN	N	norm	...
SN 2006ax	CfA	0.01671	0.01796	0.050	CN	N	norm	NIR
SN 2006bt	CSP-I	0.03217	0.03248	0.050	CL	N	norm	NIR
SN 2006bt	CfA	0.03217	0.03248	0.050	CL	N	pec	UV+NIR
SN 2006et	CSP-I	0.02217	0.02118	0.019	CN	N	norm	NIR
SN 2006gt	CSP-I	0.04477	0.04364	0.037	CL	91bg	91bg	UV+NIR
SN 2006gz	CfA	0.02370	0.02478	0.023	SS	pec	pec	NIR
SN 2006kf	CSP-I	0.02127	0.02080	0.247	CL	N	norm	...
SN 2006le	CfA	0.01742	0.01729	0.408	CN	N	norm	UV
SN 2006ob	CSP-I	0.05923	0.05825	0.033	—	—	norm	UV+NIR
SN 2006ot	CSP-I	0.05292	0.05215	0.018	BL	HV	pec	UV+NIR
SN 2007S	CSP-I	0.01385	0.01502	0.028	SS	91T	91T	...
SN 2007ai	CSP-I	0.03166	0.03199	0.332	SS	91T	91T	UV+NIR
SN 2007as	CSP-I	0.01757	0.01790	0.142	BL	HV	norm	...
SN 2007ba	CSP-I	0.03849	0.03906	0.038	CL	91bg	91bg	UV+NIR
SN 2007bd	CSP-I	0.03095	0.03194	0.034	BL	HV	norm	NIR
SN 2007jg	CSP-I	0.03710	0.03658	0.107	BL	HV	norm	UV+NIR
SN 2007nq	CSP-I	0.04503	0.04390	0.035	BL	HV	norm	NIR
SN 2008bc	CSP-I	0.01508	0.01571	0.263	CN	N	norm	NIR
SN 2008bq	CSP-I	0.03395	0.03444	0.090	CN	N	norm	NIR
SN 2008hv	CSP-I	0.01252	0.01358	0.032	CN	N	norm	NIR
SN 2008ia	CSP-I	0.02198	0.02260	0.228	BL	N	norm	...

^a Limited coverage in specific wavelength ranges: none, NIR, late-time U/u (at phases $> +20$ days), or both.

of Mandel, Narayan & Kirshner (2011). Nine of these also appear in our bolometric light curve sample. Like the SNOOPY “color model” of Burns et al. (2014), BAYESN is a hierarchical Bayesian light curve fitter designed to fit simultaneously for $E(B - V)_{\text{host}}$ and $R_{V,\text{host}}$ given optical and, when available, NIR photometry. Although BAYESN can handle different prior constraints between $E(B - V)_{\text{host}}$ and $R_{V,\text{host}}$, including the Gaussian bin prior (see “Case 6” of Mandel, Narayan & Kirshner 2011), the published extinction parameters from Mandel, Narayan & Kirshner (2011) assume that $R_{V,\text{host}}$ varies linearly with $E(B - V)_{\text{host}}$. This constraint enables the fit to combine information about $R_{V,\text{host}}$ among all SNe Ia, rather than only those with similar $E(B - V)_{\text{host}}$ values as SNOOPY does. BAYESN also uses the

Cardelli, Clayton & Mathis (1989) extinction law, while SNOOPY uses the Fitzpatrick (1999) extinction law.

The agreement between SNOOPY and BAYESN will be sensitive to differences between their training sets and priors, and serves as another cross-check on systematic errors in extinction. Figure 2 shows the difference between the values of key extinction parameters as inferred from CfA light curve data using both SNOOPY and BAYESN. Results from the two fitters agree to within RMS dispersion of 0.07 mag in $E(B - V)_{\text{host}}$ and 0.30 mag in B_{max} . The mean residuals in $E(B - V)_{\text{host}}$ and B_{max} are consistent with zero for all SNe. The main difference between the two fitters is that the BAYESN results cluster in the range $R_{V,\text{host}} \sim 2-3$, with small uncertainties compared to SNOOPY; we can attribute this to BAYESN’s stronger priors on allowed values of $R_{V,\text{host}}$, and

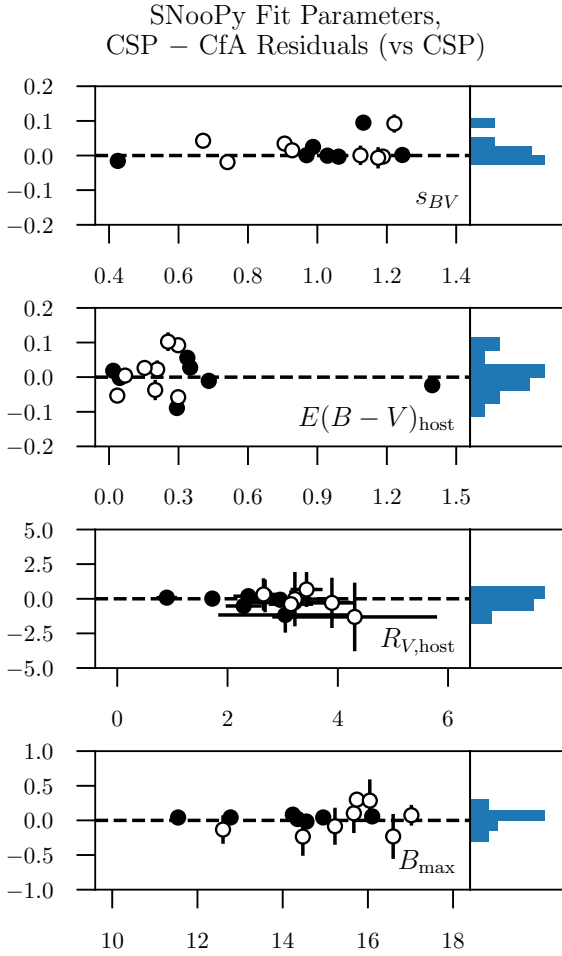


Figure 1. Comparison of SNOOPY light curve fit parameters based either on CSP-I or CfA photometry for a set of 15 SNe Ia. Open circles are points for which NIR data are unavailable in one or both surveys, while filled circles are those with NIR data from both CSP-I and PAIRITEL. Comparisons are shown (top to bottom) for s_{BV} , $E(B - V)_{\text{host}}$, $R_{V,\text{host}}$, and B_{max} .

to the extinction law used. While our fiducial results will rely on SNOOPY, we run a separate inference of M_{ej} and M_{Ni} using extinction parameters from BAYESN wherever results from both fitters are available and disagree significantly.

4 BOLOMETRIC LIGHT CURVE CONSTRUCTION

Even with excellent broadband photometry, the bolometric light curve is not directly observed, but is derived from simultaneous multi-wavelength data. Despite the stringent selection criteria laid out in §2, sampling of light curves is still often irregular, with optical and NIR observations being made on different telescopes at different times. Coverage at UV or NIR wavelengths is sometimes missing entirely and must be predicted using a plausible model of the time-evolving SED.

We rely on Gaussian process (GP) regression (Rasmussen & Williams 2005), which was used previously by Scalzo et al. (2014a) in similar ways both for interpolation in time and template correction for unobserved flux. We estimate the error introduced by interpolating or imputing over missing data by

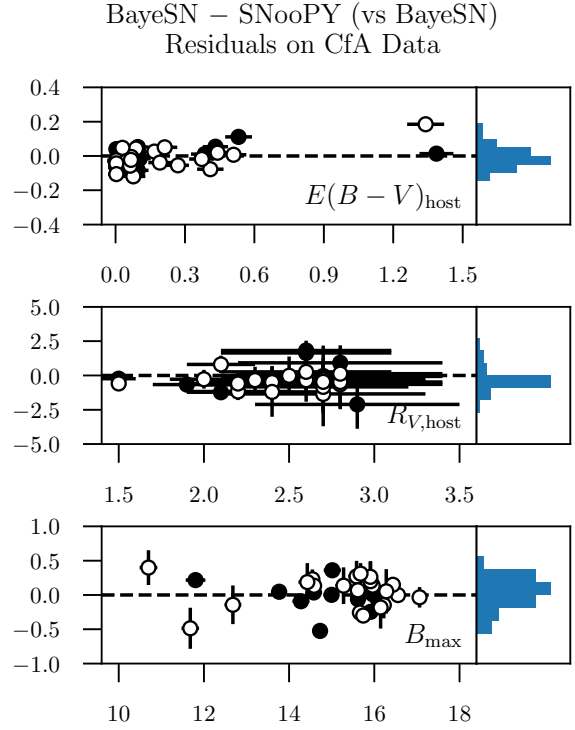


Figure 2. Comparison of host galaxy dust extinction parameters based on CfA photometry for the SNOOPY and BAYESN light curve fitters. Open circles: SNe Ia with no NIR data from PAIRITEL; filled circles: SNe Ia with PAIRITEL data. Top: $E(B - V)_{\text{host}}$. Middle: $R_{V,\text{host}}$. Bottom: B_{max} .

deleting data points from the light curves of the targets with the best coverage and repeating the analysis.

4.1 Interpolation and accounting for missing data

The behavior of a GP as a smooth non-parametric fit is governed by a mean function (which could be a parametric curve such as a polynomial) and a covariance kernel that describes correlations between the residuals of neighboring points from the mean function. Any subset of points selected from a GP are jointly (multivariate) Gaussian distributed, with covariance matrix given by the kernel. The kernel usually has hyperparameters which either are chosen to maximize the likelihood, or marginalized over to account for all possible outcomes. In the case of a light curve fit, for example, the hyperparameter might be the characteristic time scale of variation in the light curve.

We use the SNOOPY light curve fit for each SN Ia in each band as the mean function for a one-dimensional GP,

$$m_{ij} = \hat{m}_j(t_i, \Theta) + g(t_i, \Lambda), \quad (1)$$

where m_{ij} is the observed magnitude at time t_i in band j , $\hat{m}_j(t, \Theta)$ is the SNOOPY light curve with parameters $\Theta = (s_{BV}, E(B - V)_{\text{host}}, R_{V,\text{host}})$, and $g(t, \Lambda)$ is a GP fit to the residuals $m_{ij} - \hat{m}_j(t_i, \Theta)$ with covariance kernel

$$k_{1D}(t, t') = \exp \left[-\frac{(t - t')^2}{\Lambda^2} \right]. \quad (2)$$

Random fluctuations of a given SN around the SNOOPY fit will therefore be averaged out, while consistent deviations (for example, because the target is a peculiar SN Ia) will be accounted for where data are available. At times beyond the last observation in a

given band, the model reverts smoothly to the SNOOPY fit over the correlation timescale Λ of the GP (typically 1–2 weeks). When no data in a band are available (as in NIR bands for some targets), we simply use the SNOOPY predictions for that band and their associated uncertainties.

For normal SNe Ia like those used in the SNOOPY training set (including many of the CSP-I objects we analyze here), systematic variations should be minimal. For peculiar SNe Ia with missing data in wavelength or phase regions that may deviate from the SNOOPY template, we make additional arguments about how large a deviation from the SNOOPY template is needed to qualitatively change our conclusions.

Figure 3 demonstrates the procedure on SN 2004ef, a typical CSP-I SN Ia. Where data are available, the model interpolates smoothly through them, and tracks the SNOOPY template in bands and for time periods where they are unavailable — in this case, for the NIR bands after day +30.

4.2 Correction for unobserved ultraviolet flux

The potential variation of the UV contribution to the bolometric flux is illustrated by two contrasting examples of well-sampled light curves with *Swift* coverage. For the normal SN 2011fe (Pereira et al. 2013), flux in the range 1600–3400 Å increased from the earliest measured phases to reach a maximum of 13% of total bolometric flux at day –6, and was close to 10% near B maximum. For the 1991T-like SN Ia LSQ12gdj (Scalzo et al. 2014b), flux in this window made up 27% of total bolometric flux at day –10, declining to 17% by B maximum and steadily thereafter.

Our targets do not in general have *Swift* observations, so we built a UV SED template to correct for the missing flux. Building a time-dependent SED template to correct for unobserved UV flux is a challenging process, and several compromises are made; given the diversity in UV light curve behavior, we expect to capture only the distribution of possible UV corrections for a given SN Ia. We derive the correction from a separate set of SNe Ia observed with *Swift*.

A description of the full time-dependent UV correction is given in the Online Supplementary Material (S1). Its effect is small (less than 5% of bolometric flux) after day +20. Near maximum light, neither s_{BV} nor v_{Si} are good predictors of the UV flux correction — the latter potentially of interest due to the “NUV-red”/“NUV-blue” subclasses posited by Milne et al. (2013). Its main influence is therefore as a systematic error on bolometric flux at maximum light, which for purposes of deriving ^{56}Ni mass can be treated as random.

Figure 4 shows the distribution of UV flux fraction within 3 days of the date of maximum light from the SNOOPY fit. The distribution peaks around 0.08 (with mean 0.07 and standard deviation 0.03), but is skewed towards lower values. The assumption by Scalzo et al. (2014a) of a uniform distribution between 0.0 and 0.1, contributing a systematic error of about 3% to M_{Ni} , is shown to be slightly biased in the mean, but not catastrophically wrong.

4.3 Building the bolometric light curves

For each target, given a suite of light curves with quasi-simultaneous measurements in a range of bands, we build the bolometric light curve by the procedure used in Scalzo et al. (2014b). We briefly summarize the process here.

Photometric measurements taken at similar times across different bands are grouped into single multi-band measurements,

each representing at least four measurements within a 0.2-day window. The GP model is evaluated in each band to interpolate missing values at the mean date of matched observations. Missing values are interpolated only for phases before day +70, since the Hsiao et al. (2007) spectrophotometric time series template, used by SNOOPY for bandpass corrections, ends at this phase.

For each multi-band measurement, a piecewise linear broad-band SED is constructed in the observed frame using the “best-fit SED” method of Brown et al. (2016), then de-redshifted to the rest frame. Full $K+S$ -corrections are not computed, since flux from one band will be shifted into neighboring bands and will still be captured in the total bolometric flux.

The resulting optical-wavelength SED is corrected for Milky Way dust extinction using the Schlafly & Finkbeiner (2011) recalibration of the Schlegel, Finkbeiner & Davis (1998) dust maps. The correction for host galaxy dust extinction is often much larger and more uncertain than the Milky Way extinction; rather than applying a single mean correction, corrected SED time series are generated to cover a grid of values of $R_{V,\text{host}}$ from 0.0–10.0 at 0.2 mag/mag intervals, and of $E(B - V)_{\text{host}}$ from 0.00–0.50 at 0.02 mag intervals. Unextinguished UV flux densities are predicted from the GP template described in §S1, normalized to the flux density point corresponding to B -band, and joined to the optical-wavelength SED. For each value of $E(B - V)_{\text{host}}$ and $R_{V,\text{host}}$, the resulting UV-optical SED is integrated from 1600–17500 Å to obtain the bolometric flux as a function of time.

As a cross-check, “leave-data-out” tests are performed, where NIR and late-time U/u points are removed from our best-covered targets, and the light curves are reconstructed and compared to the original versions at all points between day +20 and day +70 with respect to the date of maximum light from the SNOOPY fit. For our nine targets with 3300–20000 Å coverage or equivalent at all critical epochs, the bolometric flux is unchanged to less than 2% RMS. The residual distribution broadens to 3% RMS when the entire sample is considered. Some peculiar SNe Ia, such as SN 2006ot, show greater deviations of up to 10% when the template is used, demonstrating the importance of good temporal and wavelength coverage for peculiar events.

Our bolometric light curves can be found in ASCII format in the Online Supplementary Material. For the reader’s convenience in computing light curves under different estimates of $E(B - V)_{\text{host}}$, $R_{V,\text{host}}$, and distance without exhaustively tabulating all values, we provide the observer-frame, unreddened ($E(B - V)_{\text{host}} = 0.0$) time-dependent bolometric flux, $f_{\text{bol},0}(t)$, and the coefficients of a fitting formula of the form

$$\begin{aligned} \log_{10} f_{\text{bol}}(t) &= \log_{10} f_{\text{bol},0}(t) \\ &+ a_C(t) \times E(B - V)_{\text{host}} \\ &+ a_{RC}(t) \times R_{V,\text{host}} \times E(B - V)_{\text{host}} \\ &+ a_{RCC}(t) \times R_{V,\text{host}} \times (E(B - V)_{\text{host}})^2, \end{aligned} \quad (3)$$

converting to isotropic luminosity via the luminosity distance d_L ,

$$L_{\text{bol}}(t) = 4\pi d_L^2 f_{\text{bol}}(t). \quad (4)$$

The expansion provides results with an absolute deviation limited to 0.01 dex (2.3%) worst-case for $R_{V,\text{host}} < 5$ (suitable for all SNe in this paper). For $R_{V,\text{host}} < 5$ and $E(B - V)_{\text{host}} < 0.3$ mag, suitable for all except our two most reddened SNe Ia, the worst-case deviation drops to 0.004 dex (0.9%).

SN2004ef

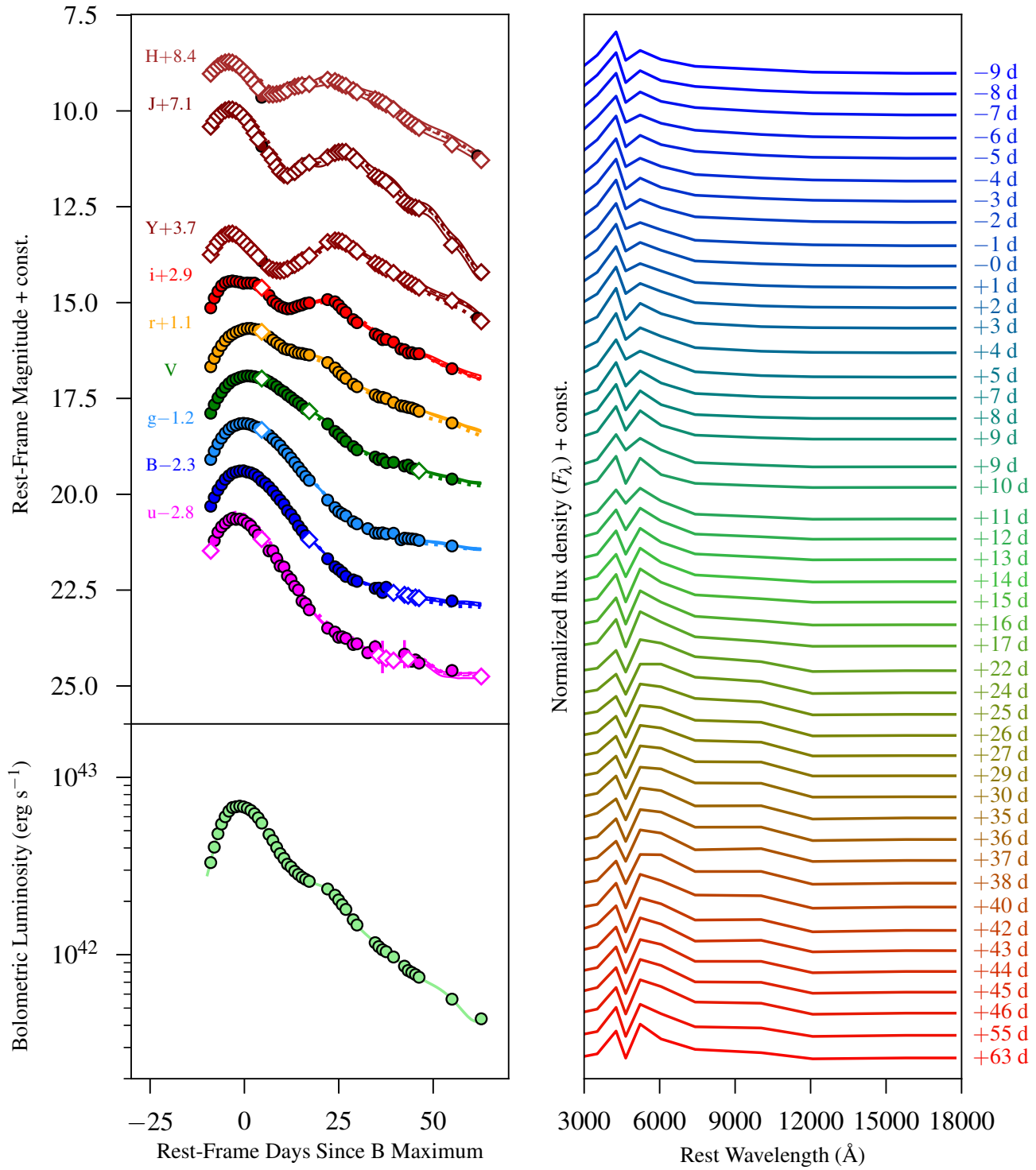


Figure 3. Construction of the bolometric light curve for SN 2004ef. Top left: broadband photometry data (filled circles) and modeled points where data are missing (diamonds). The SNOOPY fit for this SN is shown as a dotted line, and the full model taking residuals into account is shown as a dashed line with surrounding 68% confidence region. Bottom left: bolometric light curve. Right: coarse-resolution SED time series derived from broadband photometry.

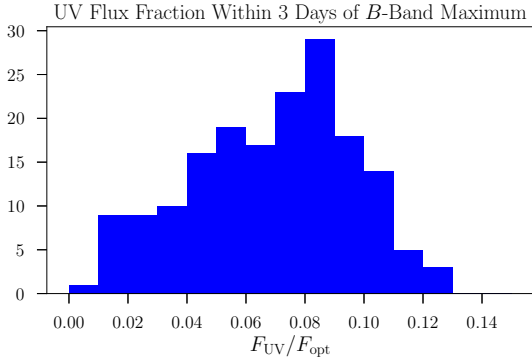


Figure 4. Ratio of UV (1600–3300 Å) to optical (3300–8500 Å) flux within 3 days of B -band maximum light.

5 MODELING PROCEDURE

For bolometric light curve modeling, we use the bolometric light curve suite BOLOMASS² (Scalzo et al. 2014a,b). BOLOMASS is a freely-available Python-based toolkit for Bayesian probabilistic inference of global SN Ia explosion properties from bolometric light curves. The inference proceeds by sampling M_{ej} , M_{Ni} , and other global properties of the white dwarf progenitor(s), explosion mechanism, and observational circumstances of each SN Ia, collectively denoted by θ . A semi-analytic forward model predicts the bolometric light curve $L_{\text{fwd,bol}}(\theta; t_i)$, which is then compared to the data $L_{\text{obs,bol}}(t_i)$ using Bayes’s rule:

$$P(\theta|L_{\text{obs,bol}}) = \frac{P(L_{\text{obs,bol}}|\theta)P(\theta)}{P(L_{\text{obs,bol}})}. \quad (5)$$

The log likelihood $\log P(L_{\text{obs,bol}}|\theta)$ is Gaussian, with mean given the forward model $L(\theta; t_i)$ and variance given by the independent observational uncertainties $\sigma_{L,i}$. The prior $P(\theta)$ encodes pre-existing knowledge about the parameters θ , which include uncertainties on “nuisance” parameters such as host galaxy reddening and distance, as well as physical constraints (such as conservation of energy, nucleosynthesis, or radiation transfer). The evidence $P(L_{\text{obs,bol}}) = \int P(L_{\text{obs,bol}}|\theta)P(\theta) d\theta$ is a normalizing constant that can be ignored as long as all models of interest lie within the parameter space spanned by θ , which can be sampled by MCMC.

The model system is a spherically symmetric, homologously expanding density distribution of ejecta. The composition is parametrized by four broad categories of elements: stable iron, ^{56}Ni , intermediate-mass elements, and unburned carbon/oxygen, lying in concentric spherical shells of density decreasing with increasing velocity. Although the model contains no hydrodynamics, it parametrizes turbulent mixing between shells by a mixing length a_{Ni} (in mass fraction coordinates) over which the composition changes smoothly from one shell to another, as in Kasen (2006). Physics such as white dwarf rotation and neutronization at high densities is also parametrized (Yoon & Langer 2005; Krueger et al. 2012). Full numerical simulations of radiation transfer in SN Ia atmospheres with similar features, such as CMFGEN (Hillier & Miller 1998; Hillier & Dessart 2012), have been quite successful in describing the overall features of SN Ia photometric and spectroscopic evolution. Where possible, we minimize model dependence by prioritizing “consensus” constraints, based on conservation laws or on correlations seen in multiple codes.

² github.com/rscalzo/pyBoloSN

In our approach, the peak luminosity contributes the most direct constraint on M_{Ni} , as in “Arnett’s rule” (after Arnett 1982). Following other authors (e.g. Branch 1992; Stritzinger et al. 2006; Howell et al. 2006, 2009), we include as a nuisance parameter the ratio $\alpha = L_{\text{max,bol}}/L_{\text{radio}} \sim 1$ of bolometric luminosity to instantaneous energy release by radioactive decay, accounting for opacity variation not captured by the Arnett (1982) model. We also take differences in rise times into account, although the full pre-explosion rise is not in general observed in our data; a prior on rise time is incorporated through its dependence on decline rate (Ganeshalingam, Li & Filippenko 2011). At late times, we approximate energy transport of ^{56}Co -decay gamma rays in the Compton-thin regime as a constant $\kappa_{\gamma} = 0.025 \text{ cm}^2 \text{ g}^{-1}$ (Swartz, Sutherland & Harkness 1995), and calculate the mean gamma-ray optical depth based on the radial distribution of ^{56}Ni (Jeffery 1999). Our model is sensitive to the ^{56}Ni distribution to at least this extent, thus sharing some features of the semi-analytic models of Pinto & Eastman (2000a), although we do not try to predict or interpret the detailed bolometric light curve pre-maximum, or between B maximum and day +40.

The capacity of the Bayesian paradigm to incorporate *informative* prior information is a double-edged sword: informative priors can reduce the posterior uncertainty, but the results may also be sensitive to the prior used. Nuisance parameters are major contributors to the final uncertainty in our inference and so our assumptions about them matter. We therefore run several different scenarios corresponding to different informative prior assumptions about the physics of radiation transfer in the expanding supernova atmosphere:

(i) Our fiducial analysis uses the “Run F” priors of Scalzo et al. (2014a), which assume $\alpha = 1$ and no dense core of iron-peak elements, and were validated in that work through a blind trial against a suite of 3-D numerical explosion models. These also produce predictions close to the median M_{ej} for the eight different priors explored in Scalzo et al. (2014a).

(ii) Two additional runs replace the assumption of $\alpha = 1$ with empirical priors that emulate ensemble-average correlations between α , ^{56}Ni content, and white dwarf central density, as estimated from the model grids of Hoefflich & Khokhlov (1996) and Blondin et al. (2013, 2017).

(iii) Finally, two additional runs under the fiducial priors modify the light curve, to evaluate the impact of potential missing flux at mid-infrared (MIR) wavelengths. These corrections are inspired by numerical simulations of Chandrasekhar-mass models, and so they may only be applicable conditional on other global parameters (e.g., $M_{\text{ej}} \sim M_{\text{Ch}}$), but are applied uniformly without regard to other parameter covariances. Our expectation based on prior experience is that an increase in late-time flux will increase the inferred mass, especially of sub-Chandrasekhar-mass candidates. We consider MIR contributions near day +60 after bolometric maximum of either 10% (estimated for normal SNe Ia) or 25% (estimated for 1991bg-like SNe Ia).

The Online Supplementary Material (S2) provides detailed justifications of each of these choices of priors and described how they were implemented.

In addition to these physical priors, we treat $E(B - V)_{\text{host}}$, $R_{V,\text{host}}$, and d_L as nuisance parameters increasing the uncertainty on M_{ej} and M_{Ni} . Our analysis calculates the luminosity distance assuming a flat Λ CDM model ($\Omega_M = 0.3$, $\Omega_{\Lambda} = 0.7$, $H_0 = 70 \text{ km s}^{-1} \text{ Mpc}^{-1}$), and a 300 km s^{-1} systematic uncertainty on the SN Ia redshift from random peculiar velocities.

We use the EMCEE package (Foreman-Mackey et al. 2013) to perform MCMC sampling over the model parameters. Scalzo et al.

(2014a) note that the posterior distribution $P(M_{\text{ej}}, M_{\text{Ni}}|\text{data})$ for any given SN Ia may be bimodal, with one mode at $M_{\text{ej}} < M_{\text{Ch}}$ and one with $M_{\text{ej}} \sim M_{\text{Ch}}$. Accordingly, we follow Scalzo et al. (2014a) in using EMCEE’s parallel-tempered MCMC sampler for our work in order to explore both modes thoroughly.

Figure 5 shows a summary of the MCMC fit for SN 2004ef under our fiducial priors. The semi-analytic expression used for the radioactive energy deposition provides an excellent description of the bolometric light curve after day +40. While α is permitted to vary, a value near 1.0 suffices to describe the data well.

6 MODELING RESULTS

Tables of the global explosion parameters inferred from our modeling, in ASCII format, can be found in the Online Supplementary Material. As in Scalzo et al. (2014a), we find a range of 0.9–1.5 M_{\odot} for M_{ej} and 0.4–1.1 M_{\odot} for M_{Ni} , with the massive, ^{56}Ni -rich end dominated by slow-declining SNe Ia (including SNe Ia spectroscopically similar to SN 1991T) and the less-massive, ^{56}Ni -poor end by fast-declining SNe Ia (including SNe Ia spectroscopically similar to SN 1991bg). Where light curves from both surveys are available, we analyze them independently, and find agreement within the uncertainty estimates given by our modeling.

6.1 Number of non-standard explosions and prior sensitivity

In the fiducial analysis, the inferences for 19 out of 41 SNe Ia show $M_{\text{ej}} < 1.4 M_{\odot}$ with $> 95\%$ probability (almost all of these at $> 99\%$ probability). For 10 other events, $M_{\text{ej}} > 1.4 M_{\odot}$ at $> 95\%$ probability, although for some of these (notably SN 2001V and SN 2005ls), the formal credible intervals are more sensitive to assumptions about host galaxy dust extinction than for the sub-Chandrasekhar-mass candidates. In the cases of SN 2006bt and SN 2006ot, the host galaxy extinction parameters from SNOOPY are believed to be unreliable, although s_{BV} may still be used as a description of the light curve shape. We re-run the fits for all of these targets under different reddening assumptions to test the robustness of our conclusions. We give more detailed comments on analysis assumptions and cross-checks for individual SNe Ia in the Online Supplementary Material (S3).

The Hoefflich & Khokhlov (1996) prior on α tends to increase the median posterior value of M_{ej} by up to 0.1 M_{\odot} , and incurs larger uncertainties on both M_{ej} and M_{Ni} . As a result, fewer individual SNe Ia are identified as non-Chandrasekhar mass at high probability than in the fiducial analysis. In contrast, the prior trained on the Blondin et al. (2017) models produces results indistinguishable from our fiducial analysis for most SNe, perhaps because it does not differ strongly from $\alpha = 1.0$ except for events with low $M_{\text{Ni}}/M_{\text{ej}}$, such as SN 2006ot.

We expect the approximate MIR flux correction to result in an increase in inferred M_{ej} , since it mainly modifies the late-time light curve. This is indeed what happens, with the fractional increase in M_{ej} being comparable to the fractional flux increase at day +60. Most (14/19) SNe Ia inferred to be sub-Chandrasekhar in our fiducial analysis remain sub-Chandrasekhar under the 10% correction. Even under the more extreme 25% correction, which should apply only to SNe Ia with luminosities and decline rates typical of the 1991bg-like subclass, three of our candidates remain sub-Chandrasekhar at a formal probability greater than 99%: SN 2000dk, SN 2006gt, and SN 2006kf.

The probability of any single SN Ia having $M_{\text{ej}} \neq M_{\text{Ch}}$ may depend sensitively on the details of the reconstruction for that SN Ia, including the priors used on the approximated explosion

Table 2. Number of expected SNe Ia in each mass bin

Prior	$N(< M_{\text{Ch}})^a$	$N(M_{\text{Ch}})^b$	$N(> M_{\text{Ch}})^c$
Run F ($\alpha = 1.0$)	22.6 ± 1.6	8.4 ± 2.2	11.9 ± 1.8
HK96 α Prior	20.3 ± 2.0	8.4 ± 2.3	14.3 ± 2.1
B17 α Prior	22.0 ± 1.4	8.5 ± 2.1	12.4 ± 1.8

Notes. Uncertainties reflect the standard deviation of counts of simulated SNe Ia within each given mass range. ^a Number of “sub-Chandra” SNe Ia with $M_{\text{ej}} < 1.35 M_{\odot}$.

^b Number of “Chandra-mass” SNe Ia with $1.35 M_{\odot} < M_{\text{ej}} < 1.5 M_{\odot}$.

^c Number of “super-Chandra” SNe Ia with $M_{\text{ej}} > 1.5 M_{\odot}$.

physics. However, we expect the total number of SNe Ia in the sample falling in different mass brackets to be more robust, since errors in M_{ej} for different SNe Ia will be independent provided that our modeling has captured covariances between M_{ej} and other variables. We assess this by drawing 1,000 simulated datasets, each containing a posterior draw of M_{ej} for each SN Ia, under each of the three priors. Following Scalzo, Ruiter & Sim (2014), for each dataset the simulated M_{ej} values are binned in three bins corresponding roughly to different explosion scenarios: “sub-Chandra” (below 1.35 M_{\odot}), “Chandra-mass” (1.35–1.5 M_{\odot} , allowing for rapid rotation), and “super-Chandra” (above 1.5 M_{\odot}). The results are listed in Table 2; there is little variation in the *total* predicted number of SNe Ia in each mass bin.

6.2 M_{ej} and M_{Ni} vs. multi-band light curve width parameters

Figure 6 shows correlations of M_{ej} and M_{Ni} with SALT2 x_1 and SNOOPY s_{BV} . The top two panels also include the fiducial values of M_{ej} and M_{Ni} as functions of x_1 for the SNfactory sample of Scalzo et al. (2014a). For normal SNe Ia, all of these correlations can be described by fits to simple linear relations.

We update our fitting formulae using our fiducial reconstructions for all spectroscopically normal SNe Ia, excluding high- ^{56}Ni outliers: the SNfactory light curves of SN 2005el and SNF 20070701-005, which were previously excluded in Scalzo et al. (2014a), and the CfA light curve of SN 2005ls, which has uncertain reddening and at-maximum spectroscopic behavior. Fitting the remaining 42 data points yields

$$M_{\text{ej}} = (1.291 \pm 0.014) + (0.196 \pm 0.011) x_1 \quad (6)$$

with $\chi^2/\nu = 28.6/43 = 0.72$, and

$$M_{\text{Ni}} = (0.659 \pm 0.023) + (0.136 \pm 0.019) x_1 \quad (7)$$

with $\chi^2/\nu = 63.3/43 = 1.06$. The parametrizations of other commonly used light curve fitters (SIFTO s , MLCS2k2 Δ) can be smoothly transformed to and from x_1 , enabling these linear relationships to be transferred readily into analogous results for other light curve fitters.

Since SNOOPY s_{BV} does not map uniquely or smoothly to and from x_1 , we fit new relations here. The best-fit linear relations for M_{ej} and M_{Ni} vs. s_{BV} , using only CSP-I + CfA data for which the light curve fits are available, is

$$M_{\text{ej}} = (1.253 \pm 0.021) + (1.036 \pm 0.095) \times (s_{BV} - 1) \quad (8)$$

($\chi^2/\nu = 27.0/24 = 1.12$), and

$$M_{\text{Ni}} = (0.718 \pm 0.027) + (0.903 \pm 0.108) \times (s_{BV} - 1) \quad (9)$$

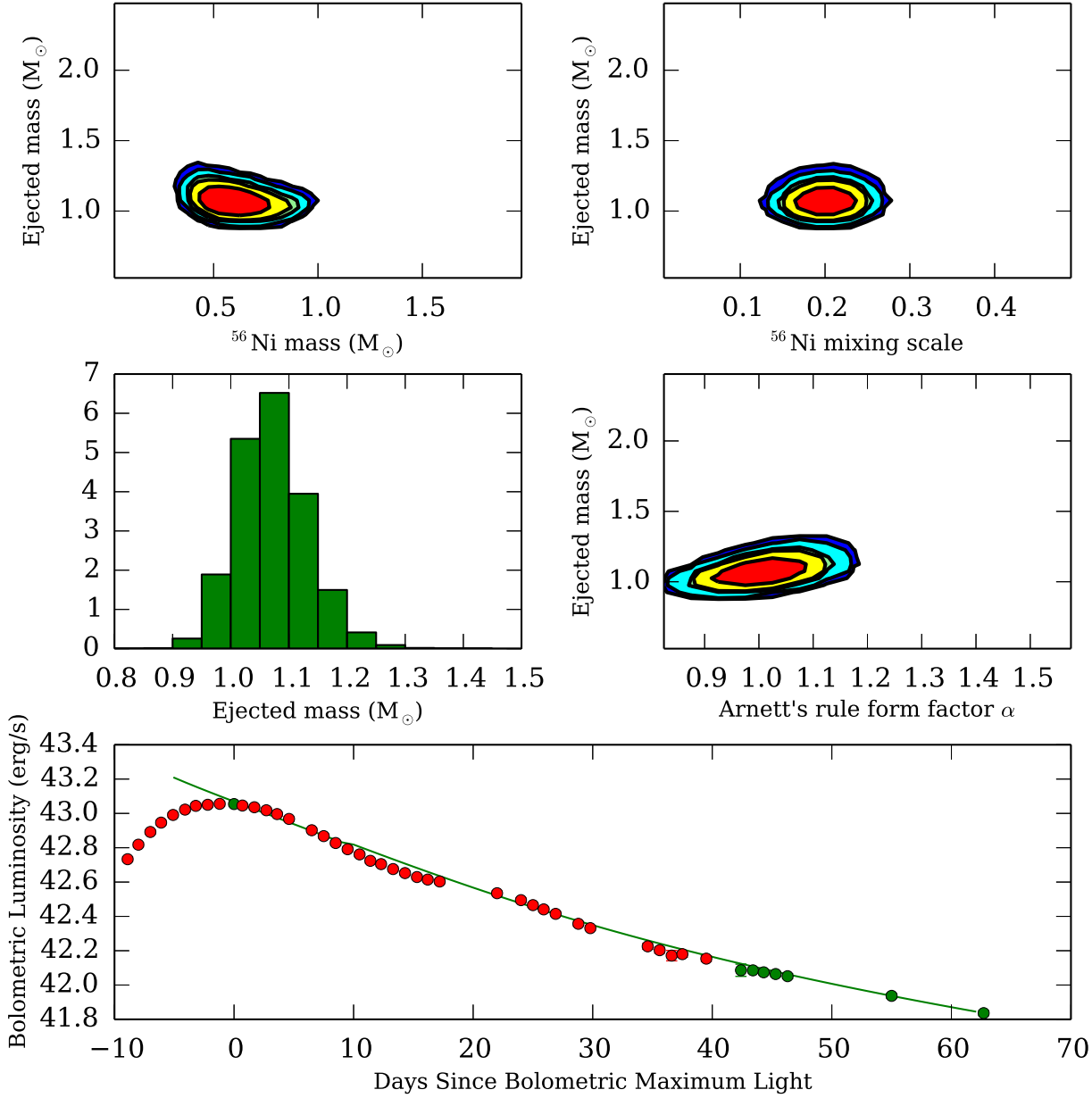


Figure 5. Confidence regions of progenitor properties for SN 2004ef. Contour plots represent projections of the full joint distribution of all parameters into the plan spanned by the panel axes. Contours bound regions of constant probability density. Colored regions, moving radially outwards, are 68% (red), 90%, 95%, 99%, and 99.7% confidence level (blue). Bottom: bolometric light curve of SN 2004ef. Green circles show which data points are included in the fit, in regions where the approximations made by the semi-analytic energy deposition model are expected to be valid; red points are excluded from the fit. The green curve shows the maximum *a posteriori* rate of radioactive energy deposition in the ejecta (multiplied by the form factor α , which is in this case close to 1, near bolometric maximum).

($\chi^2/\nu = 18.4/24 = 0.77$). The targets are not distributed uniformly along the s_{BV} axis, and so it remains unclear whether the underlying true dependence of M_{ej} on s_{BV} might be more complex; for example, a step-function transition from $M_{ej} = 1.00 M_{\odot}$ to $M_{ej} = 1.39 M_{\odot}$ around $s_{BV} = 0.9$ describes the data equally well ($\chi^2/\nu = 25.8/23 = 1.12$). Additional data could in the future clarify the functional form, and determine whether the photometric regularities picked up by s_{BV} are reflected in the inferred global physical parameters of the explosion.

6.3 M_{ej} vs. SN spectroscopic properties

Figure 7 shows the sample broken down by Branch et al. (2006) spectroscopic subtype and by v_{Si} , which determines membership in the Wang et al. (2009) “normal” (N) and “high-velocity” (HV) subtypes. The Branch type is a good predictor of which quadrant of the top panel each SN falls into. Shallow-silicon (SS) events are consistently Wang-N events with inferred $M_{ej} \geq M_{Ch}$, while core-normals (CN) and cool-photosphere (CL) events are consistently Wang-N events with $M_{ej} \leq M_{Ch}$. Broad-line (BL) events map

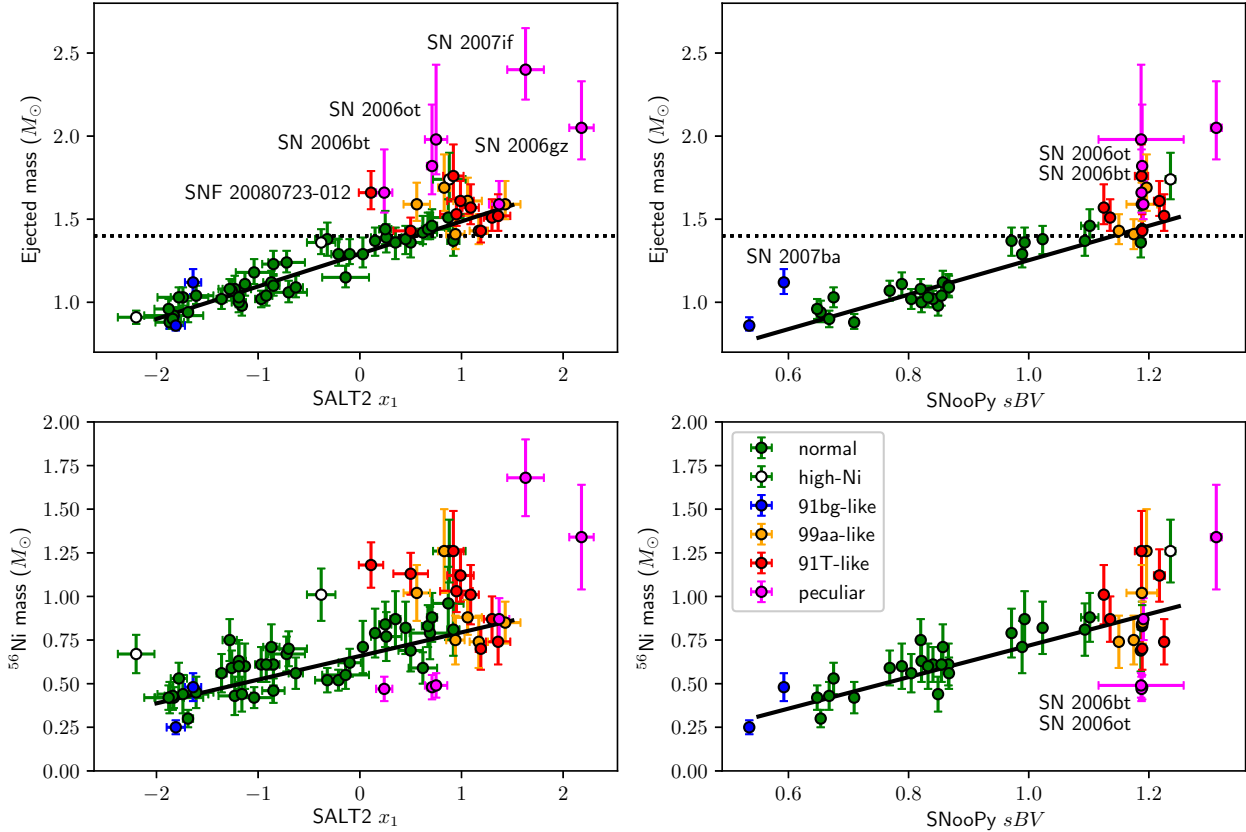


Figure 6. Ejected mass M_{ej} (top) and ^{56}Ni mass M_{Ni} (bottom) plotted against SALT2 x_1 (left) and SNOOPY s_{BV} (right). Colors show different spectroscopic subtypes as revealed by SNID: 1991T-like (red), 1999aa-like (orange), normal (green); 1991bg-like (blue); and other peculiar (magenta). The open points represent spectroscopically normal SNe Ia with anomalously high inferred M_{Ni} , which have been excluded from the best-fit linear trend(s).

well to the Wang-HV subclass, and cluster within a narrow range of sub-Chandrasekhar masses, with the exception of SN 2006ot.

The bottom panel of Figure 7 compares the inferred kinetic energy velocity v_{KE} to the measured v_{Si} , which is often used as a proxy for kinetic energy in the literature (e.g., Foley & Kasen 2011). Little correlation is seen between the two (Pearson rank $r = 0.09$); apart from the split between Wang-N and Wang-HV subclasses, v_{Si} seems to be a better predictor of the density and ionization state of the outer layers of ejecta above the Si II layer than the velocity of the bulk ejecta underneath it.

6.4 M_{ej} vs. host galaxy properties

In Figure 8 we plot the ejected masses for our sample against the stellar masses of their host galaxies. We see that SNe Ia with low-mass progenitors appear in high-mass galaxies, while low-mass galaxies tend to produce SNe Ia with more massive progenitors. This is the expected result given the correlation of ejected mass with stretch and the well-established correlation of stretch with host galaxy mass (e.g. Branch & van den Bergh 1993; Hamuy et al. 1996, 2000; Howell et al. 2009).

Interestingly, Figure 8 may indicate that SNe Ia transition from being predominantly Chandrasekhar-mass to predominantly sub-Chandrasekhar-mass at a host galaxy mass scale of about $\log(M/M_{\odot}) \sim 10.5$. Childress, Wolf & Zahid (2014) showed that the mean ages of SNe Ia also undergoes a sharp transition around the same galaxy mass scale. This would indicate that the ejected

mass (i.e. progenitor mass) and thus stretch may be driven by the age of the SN Ia progenitor system. This has been suggested in the past (e.g., Hamuy et al. 1996; Howell 2001), with proposed explanations such as the age dependence of a white dwarf’s carbon-to-oxygen ratio (Umeda et al. 1999).

6.5 Trends with bolometric light curve morphology

We now turn to correlations between M_{ej} , M_{Ni} , and morphological properties of bolometric light curves:

- (i) the bolometric luminosity $L_{\text{max,bol}}$;
- (ii) the late-time luminosity $L_{40,\text{bol}}$;
- (iii) the bolometric light curve decline rate $\Delta m_{15,\text{bol}}$, measured as the difference between the magnitude at bolometric maximum and 15 days after bolometric maximum;
- (iv) the late-time decline rate $\Delta m_{40,\text{bol}}$, defined similarly with respect to the luminosity 40 days after bolometric maximum;
- (v) $t_{+1/2}$, the time in days for the bolometric luminosity to decline from maximum to one-half maximum luminosity;
- (vi) $t_{-1/2}$, the time in days for the bolometric luminosity to rise from one-half maximum to maximum luminosity (where light curve completeness at early phases permits).

These properties are measured by evaluating the GP-based residual model directly at the required epochs, using it to interpolate smoothly in time. Marginalizing the model over $E(B - V)_{\text{host}}$ and $R_{V,\text{host}}$ shows that the variation is at or beneath the system-

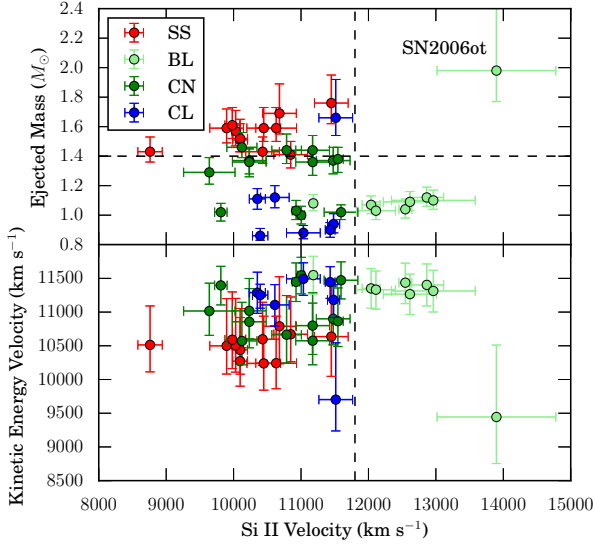


Figure 7. Ejected mass (top) and inferred kinetic energy velocity (bottom) vs. Si II velocity v_{Si} at B -band maximum light. Colors represent Branch et al. (2006) spectroscopic subtype: shallow-silicon (SS; red), broad-line (BL; light green), core-normal (CN; dark green), and cool-photosphere (CL; blue). The dashed horizontal line at top marks $M_{\text{ej}} = M_{\text{Ch}}$. The dashed vertical line marks the boundary between the Wang et al. (2009) “normal” and “high-velocity” subtypes.

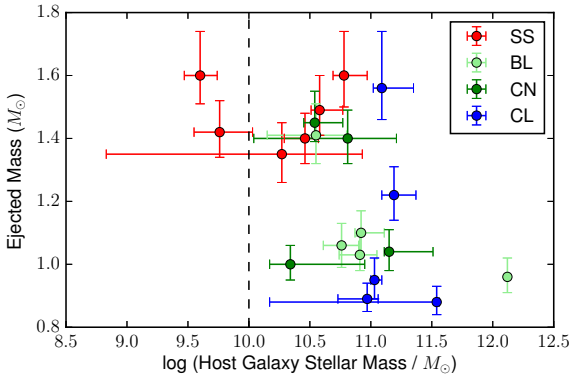


Figure 8. Ejected mass vs. host galaxy stellar mass. Colors of markers indicate the same Branch types as in Figure 7 above. The dashed vertical line at $M_{\text{host}} = 10^{10} M_{\odot}$ marks the division between “low-mass” and “high-mass” galaxies used in contemporary cosmology analyses (e.g., Betoule et al. 2014).

atic error floor of 3% established by the leave-data-out comparisons. The Online Supplementary Material contains these measurements for bolometric light curves in the present work, for the published SNfactory bolometric light curves from Scalzo et al. (2014a) (though with a larger systematic error of 0.1 mag on $\Delta m_{15,\text{bol}}$ due to the choice of parametrization for the NIR corrections), and of synthetic bolometric light curves from a suite of 3-D explosion models under various scenarios spanning a range of M_{ej} and M_{Ni} (Kromer et al. 2010; Pakmor et al. 2012; Ruiter et al. 2013; Seitzzahl et al. 2013b). In total, 63 real SNe Ia and 8 models are shown.

Figure 9 shows that $\Delta m_{40,\text{bol}}$ is an excellent predictor of M_{ej} , as suggested by figure 6 of Scalzo et al. (2014a) but not made explicit. The extremely high-mass SNe Ia (SN 2006bt, SN 2006ot, SN 2006gz and SN 2007if) all have $\Delta m_{40,\text{bol}} < 1.6$, separated from the normal and 1991T-like SNe Ia, which all have $\Delta m_{40,\text{bol}} > 1.7$. The explosion models lie along roughly the same locus as the real SNe Ia, although the three lines of sight for the asymmetric violent merger model 11+09 (Pakmor et al. 2012) show more variation than the Chandrasekhar-mass and sub-Chandrasekhar-mass models, which are closer to being spherically symmetric.

For the real SNe Ia, Figure 9 also shows a strong correlation between M_{ej} and $\Delta m_{15,\text{bol}}$ ($r = -0.905$): all $M_{\text{ej}} < M_{\text{Ch}}$ SNe Ia have $\Delta m_{15,\text{bol}} > 0.75$, and all SNe Ia with $\Delta m_{15,\text{bol}} > 0.95$ have $M_{\text{ej}} < M_{\text{Ch}}$. A matching correlation between $\Delta m_{15,\text{bol}}$ and $\Delta m_{40,\text{bol}}$ ($r = 0.929$) captures the same behavior as a geometric invariant of the bolometric light curve, independent of our interpretation of $\Delta m_{15,\text{bol}}$ or $\Delta m_{40,\text{bol}}$ in terms of M_{ej} . The 3-D explosion models shown here all have $\Delta m_{15,\text{bol}} < 0.75$ (compared with 10/63 real SNe Ia) and show no clear correspondence between $\Delta m_{15,\text{bol}}$ and M_{ej} . However, Blondin et al. (2017) find a $M_{\text{ej}}-\Delta m_{15,\text{bol}}$ relation in their grid of 1-D NLTE models, with sub-Chandrasekhar-mass models showing $\Delta m_{15,\text{bol}} > 0.8$.

The correlation between $\Delta m_{15,\text{bol}}$ and $\Delta m_{40,\text{bol}}$ is intriguing. Light curve behavior at phase +15 days depends upon a rapidly changing, temperature-dependent optical line scattering opacity, while at phase +40 days it is more stable and driven by gamma-ray opacity. The global parameters shaping light curve behavior in both regimes are M_{ej} and v_{KE} . Near maximum light, Arnett (1982) assumes a constant gray mean flux opacity κ to derive a light curve width timescale

$$\tau_m = \sqrt{\frac{2\kappa M_{\text{ej}}}{\beta c v_{\text{KE}}}}, \quad (10)$$

where $\beta \approx 13.7$ is a dimensionless factor describing the mass density profile. At late times, Jeffery (1999) use a gray mean gamma-ray scattering opacity to derive the transparency timescale

$$t_0 = \sqrt{\frac{\kappa_{\gamma} Q M_{\text{ej}}}{4\pi v_{\text{KE}}^2}}, \quad (11)$$

where Q is a dimensionless factor depending on the density profile and ^{56}Ni distribution. Taking the ratio we find

$$\tau_m/t_0 = \sqrt{\frac{v_{\text{KE}} \kappa_{\gamma} Q}{3\kappa c}}, \quad (12)$$

which is independent of M_{ej} . In this expression, c is a constant, $v_{\text{KE}}^{1/2}$ varies by at most 3% full-scale if $M_{\text{ej}} < M_{\text{Ch}}$ (see Figure 10), and $\kappa_{\gamma}^{1/2}$ is likewise nearly constant in the limit in which it is applied here (Swartz, Sutherland & Harkness 1995). Among SNe Ia with comparable density profiles, ^{56}Ni distributions, and opacity near maximum light, the ratio between the diffusion and gamma-ray transparency timescales should be nearly constant, and M_{ej} should be the primary determinant of light curve width.

Sukhbold (2018) reach a similar conclusion based on a combination of semi-analytic arguments (different from those presented above), numerical experiments, and an empirical analysis of the bolometric light curves from Scalzo et al. (2014a). However, Arnett’s expression from the diffusion time hinges on the assumption of constant mean flux opacity. Interpretation of correlations with quantities like $\Delta m_{15,\text{bol}}$ or $t_{+1/2}$ may be complicated by the rapidly changing opacity at two weeks after maximum light, as the ejecta cool and atoms recombine.

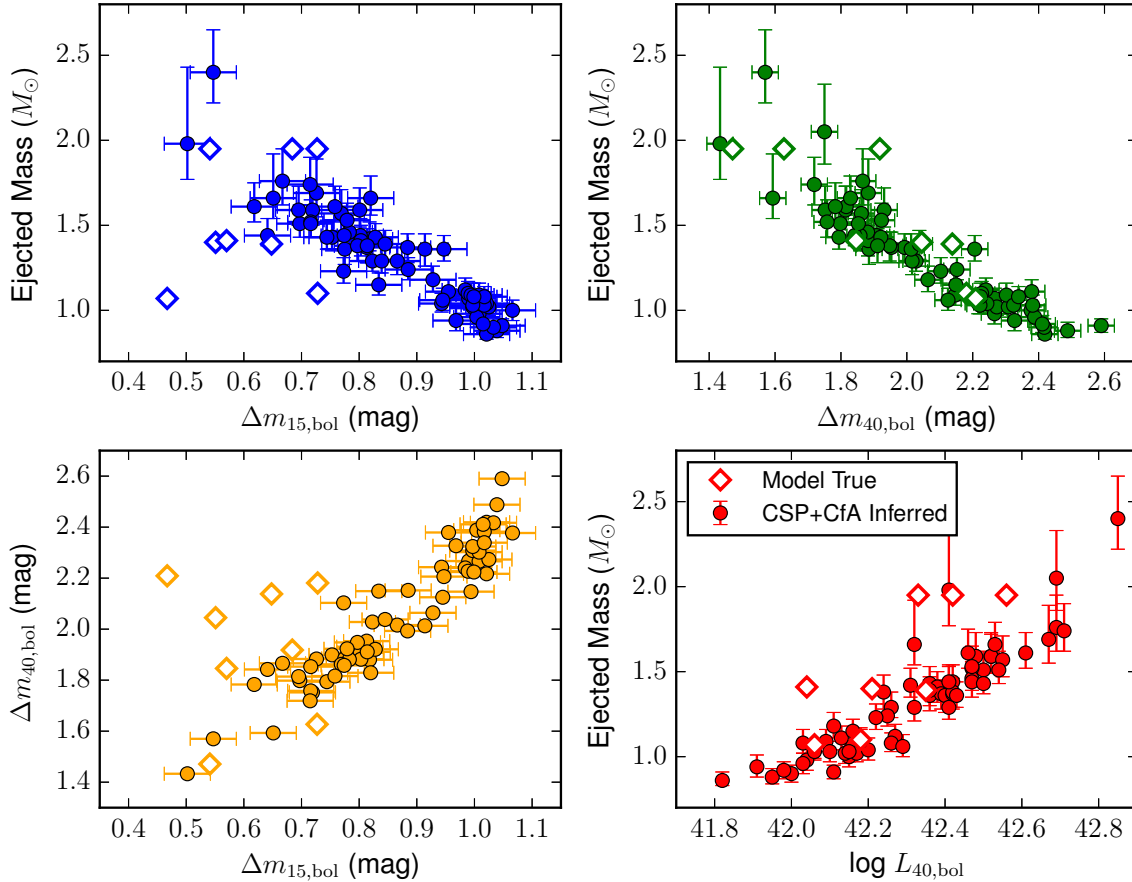


Figure 9. Correlations of ejected mass M_{ej} with bolometric light curve properties: $\Delta m_{15,bol}$ (top left), $\Delta m_{40,bol}$ (top right), and $L_{40,bol}$ (bottom right). Bottom left: $\Delta m_{40,bol}$ vs. $\Delta m_{15,bol}$. Filled circles: SN Ia data. Open diamonds: explosion models.

Using the subset of 9 SNe Ia with good early light curves, we can measure trends with $t_{-1/2}$, which depends on light curve properties in the optically thick regime, and therefore is a more direct measure of the diffusion time. Figure 11 shows plots of $t_{-1/2}$ against four main quantities of interest: $t_{+1/2}$, $\Delta m_{40,bol}$, M_{ej} , and M_{Ni} . All four quantities show correlations with $t_{-1/2}$. The explosion models once again either show no correlation or fall into different regions of parameter space from the real SNe Ia; for example, they all have $t_{+1/2} > 15$ days, while for the real SNe Ia $t_{+1/2} < 15$ days for all but one target.

Similar relations have been reported before, as early as Contardo, Leibundgut & Vacca (2000), but the point has perhaps not received as much attention as it merits. The correspondences between $t_{-1/2}$, $t_{+1/2}$, and physical properties of the explosion suggests that while energy redistribution may affect the formation of the spectrum or single-band light curves, the total energy release and shape of the light curve are governed to first order by the diffusion timescale, rather than by dramatic changes in transparency.

The details of the very early light curve within the first few days of explosion may depend upon the spatial distribution of ^{56}Ni in the outer layers, where energy can simply escape instead of diffusing (Piro & Nakar 2014; Piro & Morozova 2016). Fits of broken power laws to early light curves of some SNe Ia show breaks in the power-law index within the first few days after explosion (Zheng et al. 2013, 2014; Contreras et al. 2018). Where early light

curve data are available, extending our method to include them could provide useful constraints on the ^{56}Ni distribution we use to estimate the gamma-ray transparency of the ejecta at later times.

Turning briefly to Figure 10, the correlations between M_{Ni} , $\Delta m_{40,bol}$, and $L_{40,bol}$ also reflect the width-luminosity relation. We find a weak bolometric width-luminosity relationship by plotting $L_{max,bol}$ vs. $\Delta m_{15,bol}$ ($r = -0.526$, $p < 10^{-5}$) and M_{Ni} vs. $\Delta m_{15,bol}$ ($r = -0.568$, $p < 10^{-6}$).

7 DISCUSSION

Our analysis of a large number of new bolometric light curves are in agreement with the results of Scalzo et al. (2014a), and replicates the key finding that the ejected mass is closely linked to both the multi-band and the bolometric light curve shape. The added value lies in the diversity of peculiar objects included in our most recent analysis; in the more rigorous treatment of host galaxy dust extinction, as inferred from NIR data; and in the SNOOPY light curve parametrization, which improves the reliability of bolometric light curve modeling in the transitional period between the optically-thick and optically-thin regimes near NIR second maximum.

We discuss below what we have learned in further detail about peculiar SN Ia explosions (§7.1), the width-luminosity relation

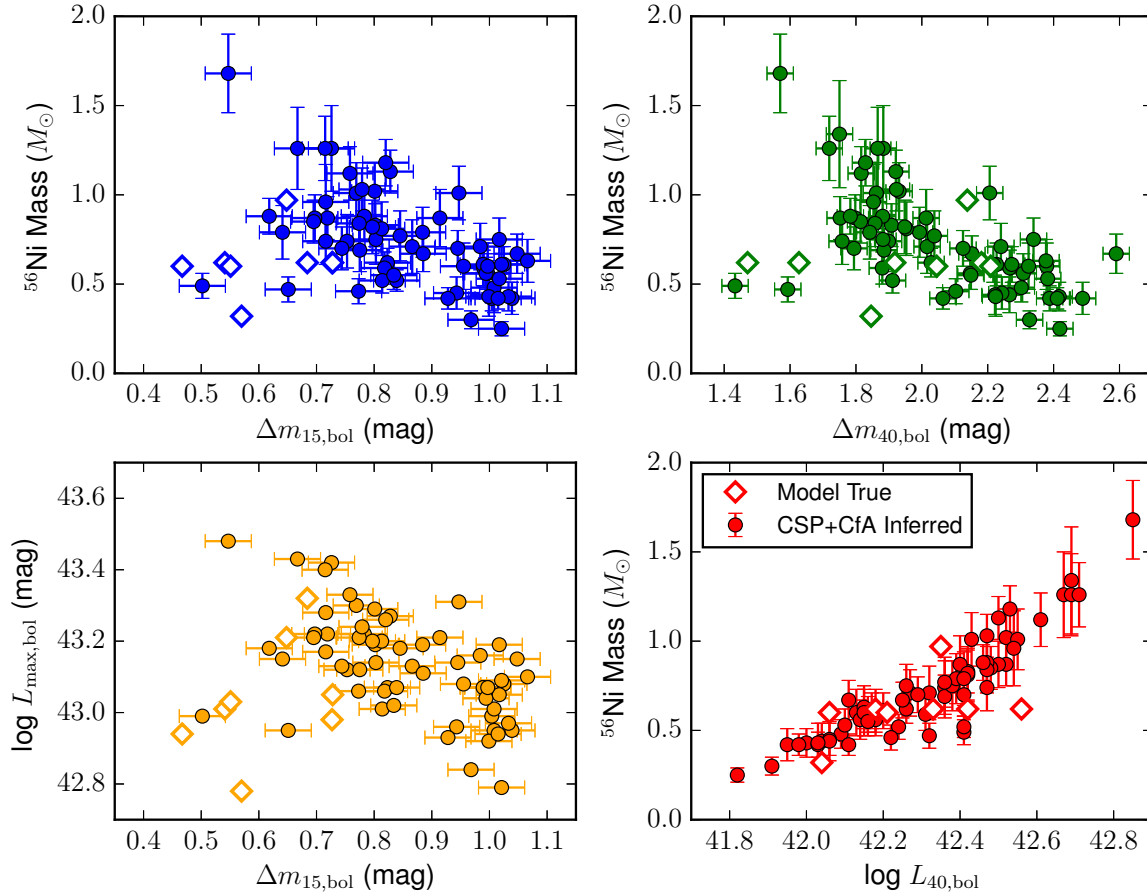


Figure 10. Correlations of ^{56}Ni mass M_{Ni} with bolometric light curve properties: $\Delta m_{15,\text{bol}}$ (top left), $\Delta m_{40,\text{bol}}$ (top right), and $L_{40,\text{bol}}$ (bottom right). Bottom left: $L_{\text{max,bol}}$ vs. $\Delta m_{15,\text{bol}}$. Filled circles: SN Ia data. Open diamonds: explosion models.

(§7.2), and the way forward for more accurate inferences about progenitors (§7.4).

7.1 Explosion mechanisms for peculiar SNe Ia

As previously found by Scalzo et al. (2012, 2014a), for 1999aa-like and 1991T-like SNe Ia we infer large ejected masses and large ^{56}Ni masses. Many of these luminous, slowly-declining SNe Ia can be plausibly explained by Chandrasekhar-mass explosions that are close to pure detonations. A few seem to have moderately super-Chandrasekhar masses $M_{\text{ej}} > 1.6 M_{\odot}$. We note that M_{ej} becomes more sensitive to assumptions about dust extinction, opacities, or distance when $M_{\text{Ni}}/M_{\text{ej}} > 0.7$; below this limit, however, the inferred value of M_{ej} becomes surprisingly robust to these assumptions, depending only on those factors which most directly influence the light curve shape. We note that our modeling assumptions are conservative in the sense that most variations, as explored in Scalzo et al. (2014a), result in comparable or higher M_{ej} for similar SNe Ia. The mass limit for rigidly rotating white dwarfs is $1.5 M_{\odot}$ (Anand 1965; Roxburgh 1965), so it may be that most 1991T-like SNe Ia share the same explosion mechanism as their spectroscopically normal counterparts.

Not all SNe Ia for which we infer $M_{\text{ej}} > M_{\text{Ch}}$ are necessarily physically related to the extreme “super-Chandra” SNe Ia with

estimated $M_{\text{ej}} > 2 M_{\odot}$ (Howell et al. 2006; Scalzo et al. 2010; Silverman et al. 2011; Taubenberger et al. 2011), which also have $M_{\text{Ni}} > M_{\text{Ch}}$ if they are powered exclusively through radioactive decay and there are no asymmetries. Our work adds SN 2006gz to the list of SNe Ia with large ejected masses inferred by this technique. However, several authors (Taubenberger et al. 2011; Hachinger et al. 2012; Taubenberger et al. 2013; Noebauer et al. 2016) argue that the extreme luminosities of super-Chandra SNe Ia are powered at least partially through shock interaction of the ejecta from a normal Chandrasekhar-mass explosion with extended circumstellar carbon-oxygen envelopes, of the kind that might be produced in double-degenerate mergers (Iben & Tutukov 1984). Our model would not describe the true physics of such an explosion, but since the required envelopes have masses of order $0.5 M_{\odot}$, the total ejecta masses are similar to the ones we infer.

Although fast-declining SNe Ia are likely to have $M_{\text{ej}} < M_{\text{Ch}}$, we find that as a class, peculiar SNe Ia with cool photospheres are not necessarily fast-declining. When the two diverge, the light curve behavior is a better predictor of M_{ej} than the spectroscopic behavior. The peculiar SN 2006bt, flagged by Foley et al. (2010) as an outlier from the width-luminosity relation for normal SNe Ia, has a cool photosphere but a broad light curve, and in our analysis reconstructs with $M_{\text{ej}} > M_{\text{Ch}}$, but with modest M_{Ni} . SN 2006ot, which Stritzinger et al. (2011) describe as photometrically similar to SN 2006bt, also shows $M_{\text{ej}} > M_{\text{Ch}}$. SN 2007ba,

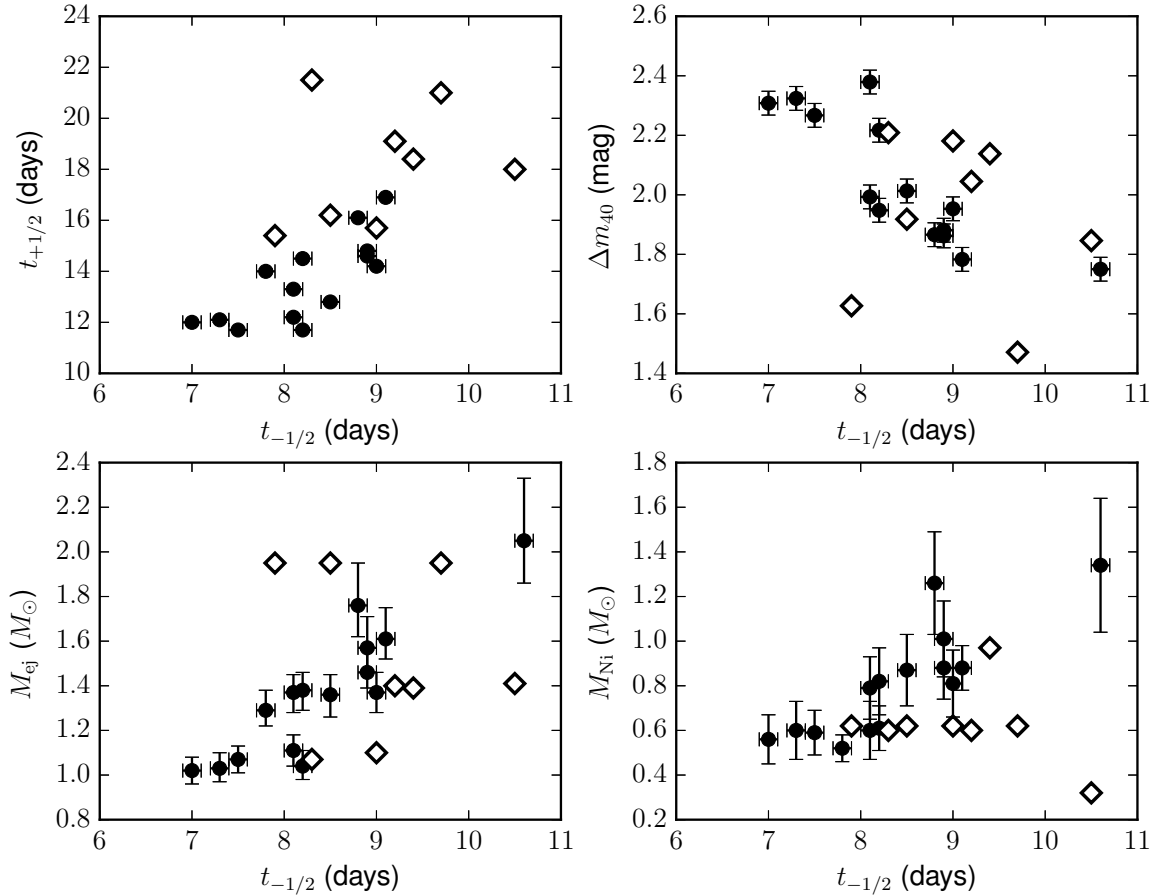


Figure 11. Correlations of half-rise time $t_{-1/2}$ with: half-decline time $t_{+1/2}$ (top left), $\Delta m_{40,\text{bol}}$ (top right), M_{ej} (bottom left), and M_{Ni} (bottom right). Filled circles: SN Ia data. Open diamonds: explosion models.

a fast-declining spectroscopic 1991bg-like SN Ia, reconstructs with $M_{\text{ej}} \sim 1.1 M_{\odot}$, still sub-Chandrasekhar but somewhat higher than other SNe Ia with similar light curve properties. There is therefore room for real physical diversity among SNe Ia with cool photospheres, and any physical theory for them must explain both photometric and spectroscopic behavior.

Most interestingly, *SN 2006bt* and *SN 2006ot* are the first SNe Ia with normal luminosities for which super-Chandrasekhar ejected masses have been inferred. The membership of SN 2006bt in the Branch-CL subclass is particularly interesting in light of the $1.66 M_{\odot}$ double-degenerate violent merger model proposed by Kromer et al. (2013) to explain the subluminous SN 2010lp, which was slowly-declining ($\Delta m_{15,B} = 1.24$) for its luminosity.

Together with the extreme “super-Chandra” SNe Ia and the 1991T-like SNe Ia, the 2006bt-like SNe Ia form a third distinct subclass of high-mass explosions. This suggests diversity in explosion mechanisms for white dwarf systems with $M > M_{\text{Ch}}$ that remains to be fully understood by mapping event classes to explosion models — for example, 2006bt-like SNe Ia to violent mergers, “super-Chandras” to explosions inside a carbon-oxygen envelope, and 1991T-like SNe Ia to single-degenerate pure detonations of spun-up white dwarfs rotating rigidly near breakup. The lack of clarity here is perhaps unsurprising given the theoretical challenges in modeling explosions of white dwarf systems with $M > M_{\text{Ch}}$,

especially the effects of magnetic fields and dynamic merger processes; we hope that our results will spur progress in this area.

7.2 Bolometric light curves and the width-luminosity relation

The use of the SNOOPY light curve fitter in this paper is not limited to improved estimates of host galaxy dust extinction. The smooth transition with increasing s_{BV} of the NIR light curves from a single-peaked to a double-peaked morphology (Burns et al. 2014) improves the reliability of our NIR corrections between the first and second NIR peaks — a range of light curve phases where the transparency of the ejecta is changing rapidly.

The resulting analysis uncovers relationships between M_{ej} , M_{Ni} , and simple morphological properties of the bolometric light curve, including a bolometric width-luminosity relation. Our inference procedure for M_{ej} uses mostly information contained in $\Delta m_{40,\text{bol}}$, and in fact does not actually use any bolometric light curve points between B maximum and day +40. There is no *a priori* reason for the ejected mass to correlate strongly with light curve behavior near day +15, but this is exactly what we find.

While existing numerical explosion models reproduce the trend between M_{ej} and $\Delta m_{40,\text{bol}}$ reasonably well, they are not guaranteed to reproduce the new correlations. No obvious trend between $\Delta m_{15,\text{bol}}$ and $\Delta m_{40,\text{bol}}$ arises from the suite of three-dimensional models shown here (Fink et al. 2010; Pakmor et al.

2012; Ruiter et al. 2013; Seitzzahl et al. 2013b). Blondin et al. (2017) note that sub-Chandrasekhar-mass models are needed to reproduce such a correlation, in addition to matching any spectroscopic properties of the resulting SNe Ia (see their figure 3), although the bolometric light curves for these models are not yet publicly available for direct comparison to our results.

Despite the strong links between M_{ej} and light curve shape, however, better predictions for M_{Ni} or for SN Ia luminosity remain elusive. The bolometric width-luminosity relation — $L_{\text{max,bol}}$ vs. either $\Delta m_{15,\text{bol}}$ or $\Delta m_{40,\text{bol}}$ — is weaker and has more scatter (0.09 dex, or 23%) than one might expect if the link between M_{ej} and M_{Ni} were as deterministic as it is in the usual double-detonation scenario (Fink et al. 2010; Sim et al. 2010; Ruiter et al. 2013). Other factors, such as the *distribution* of ^{56}Ni in the ejecta or details of radiation transfer in the transition to the optically thin regime, must also affect the observed luminosity, as has long been claimed in studies of Chandrasekhar-mass delayed detonations (e.g. Hoefflich & Khokhlov 1996; Mazzali et al. 2007) that go beyond the flux mean opacities deployed in Arnett (1982) or Pinto & Eastman (2000a). s_{BV} and similar multi-band light curve shape parameters must be sensitive to these details. Deep understanding of the physical origin of the width-luminosity relation thus awaits a physical model that can reproduce both the bolometric and multi-band observed behavior of SNe Ia.

7.3 Recent model-theory comparisons

We here review some recent developments in comparisons between theory and observations of SNe Ia, to put our work in context.

Wygoda, Elbaz & Katz (2017) re-analyze the bolometric light curves of Stritzinger et al. (2006) and Scalzo et al. (2014a) using their own numerical bolometric light curve code, inferring M_{Ni} and a transparency timescale t_0 at which the mean optical depth of the ejecta to ^{56}Co gamma rays is unity (see Jeffery 1999). The parameters as measured from their code are consistent with Scalzo et al. (2014a). They point out the importance of satisfying both the bolometric and multi-band width-luminosity relations, with their results lending support to sub-Chandrasekhar-mass double detonations and white dwarf collision models. The authors suggest that the most productive way forward is to compare M_{Ni} and t_0 directly to the output of numerical explosion models rather than to attempt an inversion, due to the model dependence of many physical details. While we agree that progress can be made by direct comparison to simulations, we believe an approach like our own also has merit: in regions of parameter space populated by multiple models, quantitative estimates of *a priori* probabilities, and of all known sources of uncertainty, are required to evaluate which model or scenario is truly the most likely.

Hoefflich et al. (2017) consider in great detail the *B*-band and *V*-band behavior of SNe Ia, demonstrating that these can be well-represented by Chandrasekhar-mass delayed detonations with varying central density and deflagration-to-detonation transition density. Ashall et al. (2018) make a similar claim for fast-declining SNe Ia, performing abundance tomography for two individual examples and measuring peak bolometric luminosities for a larger sample. Their inferences of M_{ej} for the two examples treated in detail are point estimates with large ($\sim 25\%$) formal error bars, consistent with M_{Ch} but with little discriminative power.

Blondin et al. (2017) revisit the Chandrasekhar-mass delayed detonation models of Blondin et al. (2013), while adding new Chandrasekhar-mass pulsating delayed detonation and sub-Chandrasekhar-mass double-detonation models. They note that the bolometric and multi-band properties of SNe Ia with $\Delta m_{15,B} >$

1.4 are much better explained by sub-Chandrasekhar-mass models than Chandrasekhar-mass models. Blondin, Dessart & Hillier (2018) compare in detail one of these new sub-Chandrasekhar-mass explosion models to the 1991bg-like SN 1999by, showing that it fits the observations better than the nearest competing Chandrasekhar-mass model. These results stand in sharp contrast to Hoefflich et al. (2017), although the Blondin et al. (2017) sub-Chandrasekhar-mass models still cannot reach $\Delta m_{15,B} > 1.65$.

Goldstein & Kasen (2018) present a suite of 4500 radiation transfer simulations based on parametrized ejecta models and show, in agreement with Wygoda, Elbaz & Katz (2017) and Blondin et al. (2017), that a threshold in decline rate exists below which only sub-Chandrasekhar-mass models can explain SN Ia observations. They point out that the low masses attainable by the models of Hoefflich et al. (2017) and Ashall et al. (2018) may be due in large part to substantial central cores of stable iron-peak elements in these models, which are disfavored in 3-D hydrodynamic models but are difficult to directly rule out observationally.

7.4 Bayesian inference as a way forward

Any interpretive power our technique may have in assigning values of M_{ej} and M_{Ni} to individual SNe Ia is based on Bayesian inference. We believe a Bayesian inversion approach has the potential to go beyond comparisons of point estimates of parameters for single models. Without a probability measure on the space of models, including both expert knowledge (such as those from population synthesis; Ruiter et al. 2013) and uncertainty sources (including sensitivity to initial conditions), it is hard to know whether any given model that matches observed parameters is *a posteriori* either probable or unique. Bayesian techniques also, in principle, enable the fusion of datasets and expert knowledge other than bolometric light curves (such as spectroscopy or polarimetry) for comparison to simulations, given appropriate training data.

The spatial distribution of ^{56}Ni and of stable iron-peak elements in the bulk ejecta are among the main unknowns making it difficult to reach consensus on the nature of individual SNe Ia. The potential influence of asymmetries will also need to be treated rigorously to provide the fairest possible test of explosion models such as violent mergers or white dwarf collisions. Neither the radial distribution of stable iron nor the line of sight towards an asymmetric model can be directly constrained, though they can be indirectly constrained through expensive observations such as nebular spectra (Gerardy et al. 2007; Maeda & Iwamoto 2009; Maeda et al. 2010; Maund et al. 2010). For the few SNe Ia that are nearby enough for such observations to be obtained, equally expensive forward models are required to interpret them. For SNe Ia too distant for such observations to be acquired, stable iron content and line of sight must be treated as nuisance parameters in an inversion if inferences for individual SNe Ia are to be made. Only a Bayesian approach allows for marginalization over nuisance parameters, or for statistical combination of heterogeneous types of data in a natural way.

Given the current state of affairs, semi-analytic calculations have probably reached the limits of their usefulness. More information must be brought to bear on the problem, and the natural progression from our approach would be to formulate a Bayesian inversion problem on the numerical simulations themselves. Although these simulations are expensive, hierarchical emulators could be built to quickly evaluate an approximation of their output, using as training data larger suites of simpler radiation transfer models such as those of Goldstein & Kasen (2018), and then fitting the residuals from more advanced models like those of

Blondin et al. (2017). Such an approach is out of scope of this work, but may become feasible in the near future.

8 CONCLUSIONS

We have constructed bolometric light curves for a new sample of well-observed SNe Ia located in the Hubble flow, applying the probabilistic inference framework of Scalzo et al. (2014a) to estimate their ejected masses and ^{56}Ni masses. This more than doubles the number of SNe Ia in the literature that have been analyzed by this method. The basic results of Scalzo et al. (2014a) are reproduced using a sample with a different selection function, broader wavelength coverage, and more rigorous host galaxy dust extinction estimates. The bolometric light curves are published here for use by the community.

The present work includes a more diverse sample of peculiar SNe Ia, including several well-known events and subclass exemplars. Our analysis yields at least six new SNe Ia for which $M_{\text{ej}} > M_{\text{Ch}}$ at high confidence: SN 1999dq, SN 2001V, SN 2004gu, SN 2005hj, SN 2006bt, and SN 2006ot. Our method also reproduces the anticipated large ejected mass of SN 2006gz. These events are spectroscopically diverse, with a range of ^{56}Ni masses from 0.5–1.3 M_{\odot} , but all have unusually broad light curves. The large ejected masses of SN 2006bt and SN 2006ot, relative to their ^{56}Ni production, explain why and how they deviate from the width-luminosity relation for normal SNe Ia, and make them good candidates for violent merger events. Contrariwise, cool-photosphere SNe Ia with fast-declining light curves consistently present ejected masses less than M_{Ch} . As with normal SNe Ia, these results suggest that the light curve width is a better predictor of ejected mass than spectroscopic subtype, although the details of line formation undoubtedly provide additional information about the explosion mechanism that is beyond the scope of our analysis.

Finally, correlations between morphological properties of the bolometric light curve, not reproduced fully by contemporary explosion models, provide new insight and constraints on explosion models. The relationships between inferred SN Ia ejected mass, the radiation diffusion time in the expanding ejecta, and multi-band light curve width parameters provide further evidence that variation in ejected mass is real and has a deep relationship to the standardization of SNe Ia as cosmological candles. Peculiar SNe Ia fall off of this standardization relation to the extent that they violate the underlying relationship between ejected mass and ^{56}Ni mass. Future development of explosion models focused on understanding the $M_{\text{ej}}-M_{\text{Ni}}$ relation could both yield insights into the nature of SN Ia explosions and provide better standardization relations grounded in basic physics.

ACKNOWLEDGMENTS

Parts of this research were conducted by the Australian Research Council Centre of Excellence for All-Sky Astrophysics (CAASTRO), through project number CE110001020. RS acknowledges support from ARC Laureate Grant FL0992131. We thank Ivo Seitenzahl, Brian Schmidt, Robert Kirshner, Peter Hoeflich, Bruno Leibundgut, and Suhail Dhawan for useful discussions. The CSP is grateful to the National Science Foundation for continuing support under grants AST-0306969, AST-0908886, AST-0607438, and AST-1008343.

REFERENCES

- Aldering G. et al., 2006, *ApJ*, 650, 510
 Anand S. P. S., 1965, *Proc. Natl. Acad. Sci.*, 54, 23
 Arnett W. D., 1982, *ApJ*, 253, 785
 Ashall C. et al., 2018, *MNRAS*
 Benetti S. et al., 2005, *ApJ*, 623, 1011
 Betoule M. et al., 2014, *A&A*, 568, A22
 Blondin S., Dessart L., Hillier D. J., 2018, *MNRAS*, 474, 3931
 Blondin S., Dessart L., Hillier D. J., Khokhlov A. M., 2013, *MNRAS*, 429, 2127
 Blondin S., Dessart L., Hillier D. J., Khokhlov A. M., 2017, *MNRAS*, 470, 157
 Blondin S. et al., 2012, *AJ*, 143, 126
 Blondin S., Tonry J. L., 2007, *ApJ*, 666, 1024
 Bloom J. S. et al., 2012, *ApJL*, 744, L17
 Bongard S., Baron E., Smadja G., Branch D., Hauschildt P. H., 2006, *ApJ*, 647, 513
 Bramante J., 2015, *Physical Review Letters*, 115, 141301
 Branch D., 1992, *ApJ*, 392, 35
 Branch D. et al., 2006, *PASP*, 118, 560
 Branch D., van den Bergh S., 1993, *AJ*, 105, 2231
 Breeveld A. A., Landsman W., Holland S. T., Roming P., Kuin N. P. M., Page M. J., 2011, in *American Institute of Physics Conference Series*, Vol. 1358, American Institute of Physics Conference Series, McEnery J. E., Racusin J. L., Gehrels N., eds., pp. 373–376
 Brown P. J., Breeveld A., Roming P. W. A., Siegel M., 2016, *AJ*, 152, 102
 Brown P. J., Breeveld A. A., Holland S., Kuin P., Pritchard T., 2014, *Ap&SS*, 354, 89
 Brown P. J. et al., 2009, *AJ*, 137, 4517
 Burns C. R. et al., 2014, *ApJ*, 789, 32
 Burns C. R. et al., 2011, *AJ*, 141, 19
 Cao Y. et al., 2015, *Nature*, 521, 328
 Cardelli J. A., Clayton G. C., Mathis J. S., 1989, *ApJ*, 345, 245
 Childress M. et al., 2013a, *ApJ*, 770, 108
 Childress M. et al., 2013b, *ApJ*, 770, 107
 Childress M. J., Wolf C., Zahid H. J., 2014, *MNRAS*, 445, 1898
 Chiosi E., Chiosi C., Trevisan P., Piovon L., Orto M., 2015, *MNRAS*, 448, 2100
 Chomiuk L. et al., 2016, *ApJ*, 821, 119
 Chomiuk L. et al., 2012, *ApJ*, 750, 164
 Contardo G., Leibundgut B., Vacca W. D., 2000, *A&A*, 359, 876
 Contreras C. et al., 2010, *AJ*, 139, 519
 Contreras C. et al., 2018, *ArXiv e-prints*, arXiv:1803.10095
 Davis T. M. et al., 2011, *ApJ*, 741, 67
 Dessart L., Blondin S., Hillier D. J., Khokhlov A., 2014a, *MNRAS*, 441, 532
 Dessart L., Hillier D. J., Blondin S., Khokhlov A., 2014b, *MNRAS*, 439, 3114
 Di Stefano R., Kilic M., 2012, *ApJ*, 759, 56
 Diemer B., Kessler R., Graziani C., Jordan, IV G. C., Lamb D. Q., Long M., van Rossum D. R., 2013, *ApJ*, 773, 119
 Dilday B. et al., 2012, *Science*, 337, 942
 Fink M., Röpké F. K., Hillebrandt W., Seitenzahl I. R., Sim S. A., Kromer M., 2010, *A&A*, 514, A53
 Fitzpatrick E. L., 1999, *PASP*, 111, 63
 Folatelli G. et al., 2013, *ApJ*, 773, 53
 Folatelli G. et al., 2012, *ApJ*, 745, 74
 Foley R. J., Kasen D., 2011, *ApJ*, 729, 55
 Foley R. J., Narayan G., Challis P. J., Filippenko A. V., Kirshner R. P., Silverman J. M., Steele T. N., 2010, *ApJ*, 708, 1748

- Foreman-Mackey D., Hogg D. W., Lang D., Goodman J., 2013, *Publications of the Astronomical Society of the Pacific*, 125, 306
- Friedman A. S. et al., 2015, *ApJS*, 220, 9
- Ganeshalingam M., Li W., Filippenko A. V., 2011, *MNRAS*, 416, 2607
- Garavini G. et al., 2004, *AJ*, 128, 387
- Gehrels N. et al., 2004, *ApJ*, 611, 1005
- Gerardy C. L. et al., 2007, *ApJ*, 661, 995
- Gilfanov M., Bogdán Á., 2010, *Nature*, 463, 924
- Goldhaber G. et al., 2001, *ApJ*, 558, 359
- Goldstein D. A., Kasen D., 2018, *ApJL*, 852, L33
- Guillochon J., Parrent J., Kelley L. Z., Margutti R., 2017, *ApJ*, 835, 64
- Guy J. et al., 2007, *A&A*, 466, 11
- Guy J. et al., 2010, *A&A*, 523, A7
- Hachinger S., Mazzali P. A., Taubenberger S., Fink M., Pakmor R., Hillebrandt W., Seitenzahl I. R., 2012, *MNRAS*, 427, 2057
- Hamuy M. et al., 2006, *PASP*, 118, 2
- Hamuy M. et al., 2003, *Nature*, 424, 651
- Hamuy M., Phillips M. M., Suntzeff N. B., Schommer R. A., Maza J., Aviles R., 1996, *AJ*, 112, 2391
- Hamuy M., Trager S. C., Pinto P. A., Phillips M. M., Schommer R. A., Ivanov V., Suntzeff N. B., 2000, *AJ*, 120, 1479
- Hayden B. T. et al., 2010, *ApJ*, 722, 1691
- Hicken M. et al., 2009, *ApJ*, 700, 331
- Hicken M. et al., 2012, *ApJS*, 200, 12
- Hicken M., Garnavich P. M., Prieto J. L., Blondin S., DePoy D. L., Kirshner R. P., Parrent J., 2007, *ApJL*, 669, L17
- Hillebrandt W., Kromer M., Röpke F. K., Ruiter A. J., 2013, *Frontiers of Physics*, 8, 116
- Hillier D. J., Dessart L., 2012, *MNRAS*, 424, 252
- Hillier D. J., Miller D. L., 1998, *ApJ*, 496, 407
- Hoeflich P. et al., 2017, *ApJ*, 846, 58
- Hoeflich P., Khokhlov A., 1996, *ApJ*, 457, 500
- Hosseinzadeh G. et al., 2017, *ApJL*, 845, L11
- Howell D. A., 2001, *ApJL*, 554, L193
- Howell D. A. et al., 2009, *ApJ*, 691, 661
- Howell D. A. et al., 2006, *Nature*, 443, 308
- Hsiao E. Y., Conley A., Howell D. A., Sullivan M., Pritchett C. J., Carlberg R. G., Nugent P. E., Phillips M. M., 2007, *ApJ*, 663, 1187
- Iben, Jr. I., Tutukov A. V., 1984, *ApJS*, 54, 335
- Jeffery D. J., 1999, *ArXiv Astrophysics e-prints*
- Jha S., Riess A. G., Kirshner R. P., 2007, *ApJ*, 659, 122
- Jiang J.-A. et al., 2017, *Nature*, 550, 80
- Johansson J. et al., 2017, *MNRAS*, 466, 3442
- Justham S., 2011, *ApJL*, 730, L34
- Kasen D., 2006, *ApJ*, 649, 939
- Kelly P. L., Hicken M., Burke D. L., Mandel K. S., Kirshner R. P., 2010, *ApJ*, 715, 743
- Khokhlov A., Mueller E., Hoeflich P., 1993, *A&A*, 270, 223
- Kobayashi C., Nomoto K., 2009, *ApJ*, 707, 1466
- Kromer M. et al., 2013, *ApJL*, 778, L18
- Kromer M., Sim S. A., Fink M., Röpke F. K., Seitenzahl I. R., Hillebrandt W., 2010, *ApJ*, 719, 1067
- Krueger B. K., Jackson A. P., Calder A. C., Townsley D. M., Brown E. F., Timmes F. X., 2012, *ApJ*, 757, 175
- Kushnir D., Katz B., Dong S., Livne E., Fernández R., 2013, *ApJL*, 778, L37
- Leonard D. C., 2007, *ApJ*, 670, 1275
- Li W. et al., 2011, *Nature*, 480, 348
- Li W., Filippenko A. V., Treffers R. R., Riess A. G., Hu J., Qiu Y., 2001, *ApJ*, 546, 734
- Maeda K., Iwamoto K., 2009, *MNRAS*, 394, 239
- Maeda K., Kawabata K., Li W., Tanaka M., Mazzali P. A., Hattori T., Nomoto K., Filippenko A. V., 2009, *ApJ*, 690, 1745
- Maeda K., Taubenberger S., Sollerman J., Mazzali P. A., Leloudas G., Nomoto K., Motohara K., 2010, *ApJ*, 708, 1703
- Mandel K. S., Narayan G., Kirshner R. P., 2011, *ApJ*, 731, 120
- Margutti R., Parrent J., Kamble A., Soderberg A. M., Foley R. J., Milisavljevic D., Drout M. R., Kirshner R., 2014, *ApJ*, 790, 52
- Marion G. H. et al., 2016, *ApJ*, 820, 92
- Mattila S., Lundqvist P., Sollerman J., Kozma C., Baron E., Fransson C., Leibundgut B., Nomoto K., 2005, *A&A*, 443, 649
- Maund J. R. et al., 2010, *ApJ*, 725, L167
- Mazzali P. A., Röpke F. K., Benetti S., Hillebrandt W., 2007, *Science*, 315, 825
- McWilliam A., Piro A. L., Badenes C., Bravo E., 2017, *ArXiv e-prints*
- Milne P. A., Brown P. J., Roming P. W. A., Bufano F., Gehrels N., 2013, *ApJ*, 779, 23
- Neill J. D. et al., 2009, *ApJ*, 707, 1449
- Noebauer U. M., Taubenberger S., Blinnikov S., Sorokina E., Hillebrandt W., 2016, *MNRAS*
- Nugent P., Branch D., Baron E., Fisher A., Vaughan T., Hauschildt P. H., 1995, *Physical Review Letters*, 75, 394
- Nugent P. E. et al., 2011, *Nature*, 480, 344
- Olling R. P. et al., 2015, *Nature*, 521, 332
- Pakmor R., Hachinger S., Röpke F. K., Hillebrandt W., 2011, *A&A*, 528, A117
- Pakmor R., Kromer M., Taubenberger S., Sim S. A., Röpke F. K., Hillebrandt W., 2012, *ApJL*, 747, L10
- Panagia N., Van Dyk S. D., Weiler K. W., Sramek R. A., Stockdale C. J., Murata K. P., 2006, *ApJ*, 646, 369
- Parrent J. T. et al., 2011, *ApJ*, 732, 30
- Pereira R. et al., 2013, *A&A*, 554, A27
- Perlmutter S. et al., 1999, *ApJ*, 517, 565
- Phillips M. M., 1993, *ApJL*, 413, L105
- Phillips M. M., Lira P., Suntzeff N. B., Schommer R. A., Hamuy M., Maza J., 1999, *AJ*, 118, 1766
- Pinto P. A., Eastman R. G., 2000a, *ApJ*, 530, 744
- Pinto P. A., Eastman R. G., 2000b, *ApJ*, 530, 757
- Piro A. L., Morozova V. S., 2016, *ApJ*, 826, 96
- Piro A. L., Nakar E., 2014, *ApJ*, 784, 85
- Piro A. L., Thompson T. A., Kochanek C. S., 2014, *MNRAS*, 438, 3456
- Prieto J. L. et al., 2007, *ArXiv e-prints*
- Quimby R., Höflich P., Wheeler J. C., 2007, *ApJ*, 666, 1083
- Raskin C., Scannapieco E., Rockefeller G., Fryer C., Diehl S., Timmes F. X., 2010, *ApJ*, 724, 111
- Rasmussen C. E., Williams C. K. I., 2005, *Gaussian Processes for Machine Learning (Adaptive Computation and Machine Learning)*. The MIT Press
- Riess A. G. et al., 1998, *AJ*, 116, 1009
- Riess A. G., Press W. H., Kirshner R. P., 1996, *ApJ*, 473, 88
- Roming P. W. A. et al., 2005, *Space Sci. Rev.*, 120, 95
- Röpke F. K. et al., 2012, *ApJL*, 750, L19
- Rosswog S., Kasen D., Guillochon J., Ramirez-Ruiz E., 2009, *ApJL*, 705, L128
- Roxburgh I. W., 1965, *Z. Astrophys.*, 62, 134
- Ruiter A. J. et al., 2013, *MNRAS*, 429, 1425
- Ruiz-Lapuente P., 2014, *New Ast. Rev.*, 62, 15
- Scalzo R. et al., 2012, *ApJ*, 757, 12
- Scalzo R. et al., 2014a, *MNRAS*, 440, 1498
- Scalzo R. A. et al., 2010, *ApJ*, 713, 1073
- Scalzo R. A. et al., 2014b, *MNRAS*, 445, 30

- Scalzo R. A., Ruiter A. J., Sim S. A., 2014, *MNRAS*, 445, 2535
- Schaefer B. E., Pagnotta A., 2012, *Nature*, 481, 164
- Schlafly E. F., Finkbeiner D. P., 2011, *ApJ*, 737, 103
- Schlegel D. J., Finkbeiner D. P., Davis M., 1998, *ApJ*, 500, 525
- Seitzzahl I. R., Cescutti G., Röpke F. K., Ruiter A. J., Pakmor R., 2013a, *A&A*, 559, L5
- Seitzzahl I. R. et al., 2013b, *MNRAS*, 429, 1156
- Shappee B. J. et al., 2015, *ArXiv e-prints*
- Shappee B. J., Piro A. L., Stanek K. Z., Patel S. G., Margutti R. A., Lipunov V. M., Pogge R. W., 2018, *ApJ*, 855, 6
- Shappee B. J., Stanek K. Z., Kochanek C. S., Garnavich P. M., 2017, *ApJ*, 841, 48
- Shappee B. J., Stanek K. Z., Pogge R. W., Garnavich P. M., 2013, *ApJL*, 762, L5
- Silverman J. M. et al., 2012, *MNRAS*, 425, 1789
- Silverman J. M., Ganeshalingam M., Li W., Filippenko A. V., Miller A. A., Poznanski D., 2011, *MNRAS*, 410, 585
- Silverman J. M., Kong J. J., Filippenko A. V., 2012, *MNRAS*, 425, 1819
- Silverman J. M. et al., 2013, *ApJS*, 207, 3
- Sim S. A., Röpke F. K., Hillebrandt W., Kromer M., Pakmor R., Fink M., Ruiter A. J., Seitzzahl I. R., 2010, *ApJL*, 714, L52
- Stritzinger M., Leibundgut B., Walch S., Contardo G., 2006, *A&A*, 450, 241
- Stritzinger M. D. et al., 2011, *AJ*, 142, 156
- Strolger L.-G. et al., 2002, *AJ*, 124, 2905
- Sukhbold T., 2018, *ArXiv e-prints*
- Sullivan M. et al., 2011, *ApJ*, 737, 102
- Suntzeff N. B., 1996, in *Supernovae and supernova remnants. Proceedings of the International Astronomical Union Colloquium 145; held in Xian; China; May 24-29; 1993; Cambridge; UK: Cambridge University Press; —c1996; edited by Richard McCray and Zhenru Wang, p.41, p. 41*
- Swartz D. A., Sutherland P. G., Harkness R. P., 1995, *ApJ*, 446, 766
- Taddia F. et al., 2012, *A&A*, 545, L7
- Taubenberger S. et al., 2011, *MNRAS*, 412, 2735
- Taubenberger S. et al., 2013, *MNRAS*, 432, 3117
- Thomas R. C. et al., 2011, *ApJ*, 743, 27
- Thompson T. A., 2011, *ApJ*, 741, 82
- Tripp R., 1998, *A&A*, 331, 815
- Umeda H., Nomoto K., Kobayashi C., Hachisu I., Kato M., 1999, *ApJL*, 522, L43
- Vacca W. D., Leibundgut B., 1996, *ApJ*, 471, L37
- Vinkó J. et al., 2003, *A&A*, 397, 115
- Wang B., Han Z., 2012, *New Ast. Rev.*, 56, 122
- Wang X. et al., 2009, *ApJL*, 699, L139
- Whelan J., Iben, Jr. I., 1973, *ApJ*, 186, 1007
- Wood-Vasey W. M., Wang L., Aldering G., 2004, *ApJ*, 616, 339
- Woods T. E., Gilfanov M., 2013, *MNRAS*, 432, 1640
- Woods T. E., Gilfanov M., 2014, *MNRAS*, 439, 2351
- Woosley S. E., Weaver T. A., 1994, *ApJ*, 423, 371
- Wygoda N., Elbaz Y., Katz B., 2017, *ArXiv e-prints*
- Yoon S.-C., Langer N., 2005, *A&A*, 435, 967
- Yuan F. et al., 2010, *ApJ*, 715, 1338
- Zheng W. et al., 2014, *ApJL*, 783, L24
- Zheng W. et al., 2013, *ApJL*, 778, L15

S1 TIME-DEPENDENT UV FLUX CORRECTIONS

A suite of *Swift* light curves for 115 SNe Ia with $z < 0.02$, 15 of which also had published photometry from CSP-I or CfA, were used for training. Of these, 79 had light curves sufficiently well-sampled (including *Swift* *ubv* and any optical data) to achieve a convergent SNOOPY fit. For each SN Ia at each epoch, a UV SED was constructed from the *Swift* photometry using the “best-fit SED” method of Brown et al. (2016). This method solves for a self-consistent set of flux densities in a piecewise-linear SED, constrained to produce synthetic photometry in the observed filters that best approximate the photometric observations. The method naturally accounts for the red leaks in the *Swift* UV filters, and gives results accurate at level of 2% of the integrated flux in the range 1600–6000 Å (Brown et al. 2016). Each UV-based SED was then de-reddened using the $E(B - V)_{\text{host}}$ and $R_{V,\text{host}}$ parameters from the SNOOPY fit to produce intrinsic SEDs.

Milne et al. (2013) separated *Swift* SNe Ia into “NUV-red” and “NUV-blue” subtypes, with normal-velocity (Wang et al. 2009) SNe Ia associated exclusively with the NUV-blue subtype. v_{S1} might therefore be a useful predictor of UV SED behavior for SNe Ia with no *Swift* observations. A search of the Open Supernova Catalog (Guillochon et al. 2017) yielded 25 SNe Ia with both *Swift* coverage and optical spectra within 3 days of *B*-band maximum light. From these spectra, v_{S1} was measured using the technique described in Scalzo et al. (2012), in which a pseudo-continuum is estimated by applying a Savitzky-Golay filter to the data, and uncertainties on the position of the line minimum are estimated by Monte Carlo simulation.

Figure S1 shows the ratio of UV to optical flux as a function of rest-frame light curve phase for the training set. No clear correlation of UV flux fraction with s_{BV} or with the Wang spectral type is seen; examples can be found for any light curve shape or velocity spanning nearly the full range of UV behavior.

To build a *time-dependent* template for UV flux, we normalize each SED to unit flux density at 4355 Å (the *B*-band point) and take the logarithm. We then train a GP model to predict the (log) flux density based on phase, wavelength, and s_{BV} , much like the NIR template correction used by Scalzo et al. (2014a); the covariance is

$$k_{3D}(\mathbf{x}, \mathbf{x}') = \exp [(\mathbf{x} - \mathbf{x}')^T \Theta (\mathbf{x} - \mathbf{x}')], \quad (13)$$

with feature vector $\mathbf{x} = (t, s_{BV}, \log(\lambda))$ and hyperparameters $\Theta = \text{diag}(\Theta_t, \Theta_{s_{BV}}, \Theta_\lambda)$. We choose to predict the UV SED, instead of a correction as a fraction of the optical flux, in order to capture the covariance between inferred UV flux fraction and extinction properties. This procedure ensures that uncertainties in reddening are treated self-consistently in downstream modeling.

The resulting fitted template is shown in Figure S2. While s_{BV} is not a particularly good predictor of near-UV color, the predicted *B*-band flux density at given s_{BV} provides a convenient normalization for the SED. The *Swift* $u - b$ and $b - v$ colors show the usual tight dispersion with light curve shape. For the bluer bands, the dispersion is much larger (~ 0.4 dex RMS); this full dispersion is propagated through to the final uncertainty estimation on the integrated bolometric flux.

S2 PRIORS FOR EXPLOSION PROPERTY INFERENCE

S2.1 Fiducial priors

Our fiducial modeling assumptions correspond to “Run F” of Scalzo et al. (2014a), which successfully reproduce the ejected masses of a diverse suite of three-dimensional explosion models: sub-Chandrasekhar-mass double detonations (Fink et al.

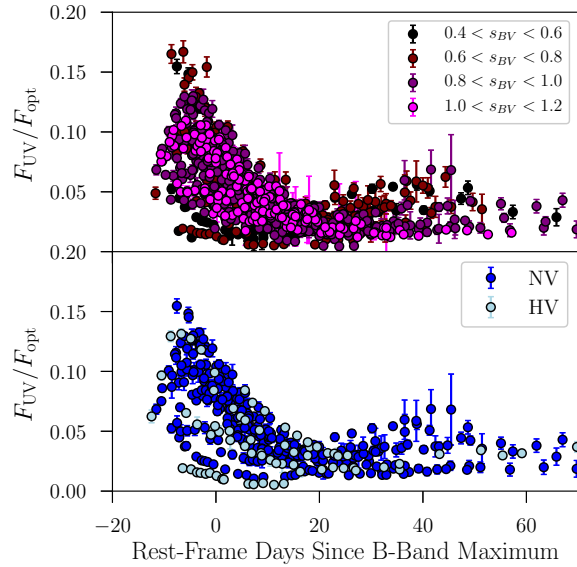


Figure S1. Ratio of UV (1600–3300 Å) to optical (3300–8500 Å) flux as a function of *B*-band light curve phase. Top: 79 SNe Ia in four bins of light curve shape — $0.4 < s_{BV} < 0.6$ (black), $0.6 < s_{BV} < 0.8$ (maroon), $0.8 < s_{BV} < 1.0$ (purple), and $1.0 < s_{BV} < 1.2$ (magenta). Bottom: 25 SNe Ia divided between the Wang et al. (2009) normal (dark blue) and high-velocity (light blue) subtypes. No clear correlation is seen of UV flux fraction with s_{BV} or Wang type is seen.

2010; Ruiter et al. 2013), super-Chandrasekhar-mass violent mergers (Pakmor et al. 2012), and Chandrasekhar-mass delayed detonations (Seitenzahl et al. 2013b). Run F assumes:

- (i) an ejecta density profile $\rho(v) \propto [1 + (v/v_{\text{KE}})^3]^{-3}$;
- (ii) no dense core of stable iron-peak elements;
- (iii) less than $0.05 M_\odot$ of unburned material; and
- (iv) $\alpha = 1.0$.

These assumptions are difficult or impossible to fully confirm observationally with current techniques, but all are motivated by one or more contemporary explosion models from different groups, and the effects of varying them are described in detail in Scalzo et al. (2014a). The density profile is the most influential factor, with different functional forms changing the absolute inferred mass scale up or down by about $0.1 M_\odot$. The form factor α affects M_{Ni} directly, and affects M_{ej} through the inferred transparency of the ejecta to ^{56}Co gamma rays. The fraction of unburned material and the presence or absence of a stable iron-peak core turn out to be less influential, affecting M_{ej} and M_{Ni} at the $0.05 M_\odot$ level or less. The Run F results are close to the median of the distribution of M_{ej} for each SN Ia obtained by varying over the eight different priors explored in Scalzo et al. (2014a).

Thus, sensitivity to priors introduces some uncertainty on the overall mass scale, as well as in the posterior variance of M_{ej} for individual SNe Ia, which may affect the interpretation of our present work. However, the range of M_{ej} values inferred for normal SNe Ia was not found to be sensitive to the choice of prior in Scalzo et al. (2014a). The existence of a correlation between M_{ej} and SALT2 x_1 is also robust: a change of prior alters the fitting formula’s intercept but has little effect on its slope.

Scalzo, Ruiter & Sim (2014) apply such a fitting formula to a larger sample of 337 SNe Ia from the Supernova Legacy Survey (Betoule et al. 2014) to infer the intrinsic distribution of M_{ej} , us-

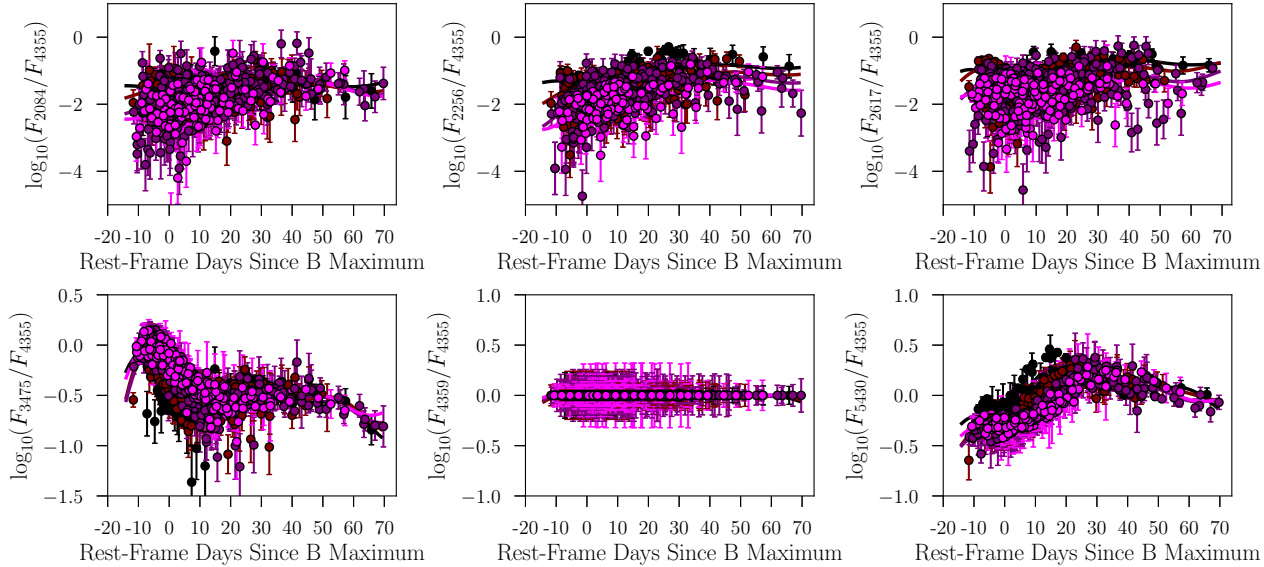


Figure S2. Log flux ratios at different wavelengths for SEDs built from *Swift* data. Colors show different ranges of s_{BV} as in the top panel of Figure S1. Bold lines with cross-hatches show Gaussian process fits, with 68% confidence regions, evaluated at the midpoint of each bin in the s_{BV} sequence.

ing it to make separate arguments that Run F is well-calibrated. The M_{ej} distribution shows a sharp peak at $1.4 M_{\odot}$, which is well-explained by Chandrasekhar-mass models, but with a tail extending down to $0.8 M_{\odot}$. Any choice of prior producing results very different from Run F would imply a peak at some other mass scale, which would require explanation by some other scenario. A peak near $1.2 M_{\odot}$ could be explained by violent white dwarf mergers (Ruiter et al. 2013), though this would result in very few Chandrasekhar-mass SNe Ia to satisfy nucleosynthetic constraints (Seitenzahl et al. 2013a). Similarly, Piro, Thompson & Kochanek (2014) note that the white dwarf collisions of Kushnir et al. (2013) would imply a peak in M_{ej} around $1.6 M_{\odot}$, given the luminosity distribution of these events as compared with normal SNe Ia.

The overall shape of the distribution (in particular, the width of the peak or the presence of a low-mass tail) will be affected only by strong systematic variations in density or maximum-light opacity as a function of decline rate. To address this possibility, the present work explores two other effects not previously considered in Scalzo et al. (2014a): more sophisticated priors on α which take into account correlations with other global parameters not accounted for in a simple Gaussian prior, and the possible influence of unobserved mid-infrared (MIR) flux on the bolometric light curve.

S2.2 Model-dependent covariances between α and other global explosion parameters

The true distribution of α is uncertain and reflects dependence on tuning to particular suites of numerical models; the details of radiation transport near maximum light are too complex to unfold fully in a semi-analytic model and must be simulated numerically. For the semianalytic models of Arnett (1982), α is exactly equal to 1, by construction. For the 1-D radiation hydrodynamic models of Hoeflich & Khokhlov (1996), α varied in the range 0.6–1.4 depending on the explosion mechanism. The 1-D models of Blondin et al. (2013, 2017) assume homologous expansion after initial burning ceases, but treat radiation transfer in non-local thermodynamic equilibrium (NLTE), leading to α in the range 0.9–1.3. To capture possible covariances between α and global explosion

parameters that are lost by using a fixed value of α or a simple Gaussian prior, we construct empirical priors from the published model grids of Hoeflich & Khokhlov (1996) and Blondin et al. (2013, 2017) as GP regressions, and simulate them for comparison with the fiducial Run F prior.

The new priors use the ^{56}Ni mass ratio M_{Ni}/M_{ej} and the white dwarf central density ρ_c as potential predictors of α , on the basis that both parameters affect the opacity (via temperature) and the radial distribution of ^{56}Ni . Since the intrinsic dispersion of α around the mean trend for each explosion model grid is unknown, we fit for it as a hyperparameter. The results for both explosion model grids are shown in Figure S3.

The GP regression for the Hoeflich & Khokhlov (1996) model grid predicts α with RMS dispersion of 17%. The input data comprise two clusters in central density: a high-density cluster of Chandrasekhar-mass delayed detonations with $\log_{10} \rho_c \sim 9.3\text{--}9.5$, and a low-density cluster of sub-Chandrasekhar-mass double detonations and super-Chandrasekhar-mass tamped detonations with $\log_{10} \rho_c \sim 7.0\text{--}7.6$. The low-density cluster has a higher mean α (1.10) than the high-density cluster (0.97). There is also a trend with ^{56}Ni mass, with a maximum in α being attained around $M_{\text{Ni}}/M_{ej} \sim 0.35$.

In contrast, the GP regression for the Blondin et al. (2013, 2017) model grid has a much smaller dispersion (2.5%), and α is determined entirely by M_{Ni}/M_{ej} . The trend with M_{Ni}/M_{ej} is also monotonically decreasing. As in the Hoeflich & Khokhlov (1996) model grid, delayed detonations, pulsating delayed detonations, and sub-Chandrasekhar-mass detonations all contribute. Blondin et al. (2013) note that the input hydrodynamic models are produced by the same code, so that the difference probably lies in different treatments of opacity and its effects on the optical depth and diffusion time.

These two contrasting cases demonstrate one of the challenges in assigning a more complex prior on α , namely, that different codes run on similar physical scenarios may obtain different results; it can be hard to tell whether regularities among models in a grid reflect true physical constraints or merely result from approximations made in each code. As the physical relationship between α

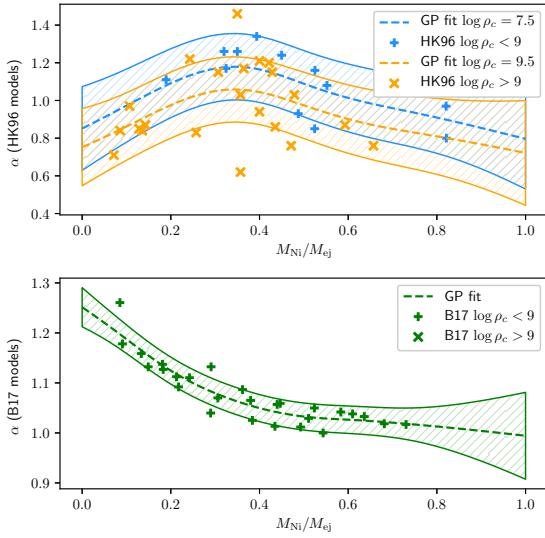


Figure S3. Variation in the form factor α for the 1-D models of Hoefflich & Khokhlov (1996) (top) and Blondin et al. (2017) (bottom). Low-density explosion models are marked with vertical crosses, and high-density explosion models by diagonal crosses. Mean GP predictions are shown as dotted lines, while the hatched regions are 68% confidence intervals. These regressions are used as priors linking α to M_{Ni} and M_{ej} in our modeling.

and global physical parameters is clarified further by future work, we can expect the uncertainty in our inferences to decrease. For the time being, because each informative prior encodes specific physics assumptions that may help to constrain the final results, we prefer to treat each one separately in order to be transparent about those assumptions, rather than using a single broad prior insensitive to underlying correlations between model parameters.

S2.3 Potential influence of unobserved MIR flux

Unobserved MIR flux is difficult to correct for, since few MIR observations of SNe Ia exist from which a template could be constructed, and since theoretical predictions of MIR emission remain uncertain. Rayleigh-Jeans extrapolations of our own SEDs suggest that unobserved MIR flux as a fraction of observed flux from 1600–17500 Å ranges from less than 5% near maximum light to around 10% near day +40, with no strong dependence on decline rate s_{BV} . As discussed above, the flux difference between maximum light and later phases is the most effective predictor of M_{ej} within our modeling framework, so uncaptured flux at late times could bias our ejected mass estimates. We cross-check this finding against empirical SEDs from data in the literature and a theoretical ansatz.

Johansson et al. (2017) provide MIR light curves of 9 normal SNe Ia with decline rates $0.9 < \Delta m_{15,B} < 1.3$ measured with the *Spitzer* space telescope; except for the well-observed SN 2014J, there are in general very few light curve points available for light-curve phases between maximum light and day +80. We used available light curve data to build SEDs at phases relevant to our analysis for two SNe Ia observed by Johansson et al. (2017): SN 2007le ($\Delta m_{15,B} = 1.10$ mag) and SN 2009ig ($\Delta m_{15,B} = 0.89$ mag). Integrated flux in the range 2–6 microns made up 5% of total bolometric flux for SN 2007le at day +66, and only 3% for SN 2009ig at day +36, in each case less than the Rayleigh-Jeans extrapolation

predicts. These two cases suggest that the effects of neglecting MIR flux are minimal compared to other systematic sources of uncertainty from factors such as distance, reddening, and model inadequacy, at least for SNe Ia on the slow-declining side of normal.

In Chandrasekhar-mass delayed detonation models of faster-declining SNe Ia, MIR contributions could be larger than this (Hoefflich, private communication). As an additional test, two new analyses were run in which the late-time bolometric flux was boosted by a linearly interpolated fraction between day +55 and day +85, based on models for normal SNe Ia (“case A”: 10% increase at day +60, 25% increase at day +80) and for 1991bg-like SNe Ia (“case B”: 25% increase at day +60, 40% increase at day +80). We caution that this ansatz applies only to one explosion scenario, and that it does not capture correlations between unobserved MIR flux and other explosion parameters. Future publications of synthetic bolometric light curves from numerical explosion models, as well as new MIR observations of SNe Ia, will enable us to examine these effects in more detail.

S3 COMMENTS ON INDIVIDUAL SUPERNOVAE

S3.1 SN 1999aa

This CfA SN Ia from Jha, Riess & Kirshner (2007) is the exemplar of its own slowly-declining subclass (Li et al. 2001; Strolger et al. 2002; Garavini et al. 2004; Silverman et al. 2012), intermediate between Branch-normal SNe Ia and 1991T-like SNe Ia. A fit to the multi-band light curve using SALT2 yields $x_1 = +1.17$, $c = -0.08 \pm 0.02$, while SNOOPY gives $s_{BV} = 1.15$ and negligible host galaxy reddening ($E(B - V)_{\text{host}} = 0.005 \pm 0.016$ mag). Its CMB-centric redshift is $z_{\text{CMB}} = 0.01522$, giving $\mu = 34.10 \pm 0.15$ mag for our assumed cosmology and peculiar velocity systematic. Given these constraints, SN 1999aa reconstructs as a moderately bright Chandrasekhar-mass event ($M_{\text{ej}} = 1.42^{+0.10}_{-0.07} M_{\odot}$, $M_{\text{Ni}} = 0.78^{+0.16}_{-0.13} M_{\odot}$).

S3.2 SN 1999dq

This CfA SN Ia from Jha, Riess & Kirshner (2007) is slow-declining ($x_1 = +0.83$, $s_{BV} = 1.20$), with a 1999aa-like spectrum (Silverman, Kong & Filippenko 2012) and significant reddening ($E(B - V)_{\text{host}} = 0.154$ mag, $R_{V,\text{host}} = 3.5$ mag), putting its corrected intrinsic color at $(B - V)_{\text{max}} = -0.12$ mag. Its CMB-centric redshift is $z_{\text{CMB}} = 0.0136$, leading to a distance modulus $\mu = 33.89 \pm 0.15$ mag for our assumed cosmology and peculiar velocity systematic. SN 1999dq reconstructs as a luminous super-Chandrasekhar-mass event at $> 95\%$ confidence ($M_{\text{ej}} = 1.67^{+0.19}_{-0.14} M_{\odot}$, $M_{\text{Ni}} = 1.28^{+0.25}_{-0.22} M_{\odot}$).

Neill et al. (2009) measure $M_{\text{Ni}} = 0.96 \pm 0.09 M_{\odot}$ for SN 1999dq (assuming zero host galaxy extinction) via the technique of Howell et al. (2009), which uses the Hsiao et al. (2007) spectroscopic template for the bolometric correction near maximum light. Correcting this zero-extinction estimate using the observed color as a proxy for reddening by dust in the host galaxy, Neill et al. (2009) measure $M_{\text{Ni}} = 1.22 \pm 0.11 M_{\odot}$ for SN 1999dq, the highest in their sample, and comparable to our own estimate.

S3.3 SN 2001V

This CfA SN Ia from Jha, Riess & Kirshner (2007) was noted by Vinkó et al. (2003) as being slow-declining and exceptionally luminous, with estimated $M_B \sim -20$ and a 1999aa-like

spectrum near maximum light. The light curve width parameters from our fits are $x_1 = 0.85$ and $s_{BV} = 1.19$. The CfA light curve is exceptionally complete and suggests a very blue SN Ia. Our inferred $A_V = 0.46 \pm 0.14$ mag is non-negligible, while Mandel, Narayan & Kirshner (2011) infer much stricter limits $A_V < 0.11$ mag (68% confidence). Our extinction estimate implies $(B - V)_{\max} = -0.19$ mag, $M_B = -20.21$ mag. However, even with no host galaxy extinction correction, $M_B = -19.72$ mag for SN 2001V, indicating a large mass of ^{56}Ni ($> 0.9 M_\odot$) without accounting for flux bluewards of B -band which can contribute substantially to the luminosity (Scalzo et al. 2014b). Using the SNOOPY extinction values, SN 2001V reconstructs as super-Chandrasekhar-mass ($M_{\text{ej}} = 1.78^{+0.20}_{-0.15} M_\odot$, $M_{\text{Ni}} = 1.29^{+0.25}_{-0.22} M_\odot$). Using the BAYESN upper limit, SN 2001V is still super-Chandrasekhar-mass at $> 95\%$ confidence ($M_{\text{ej}} = 1.60^{+0.14}_{-0.10} M_\odot$, $M_{\text{Ni}} = 0.97^{+0.18}_{-0.16} M_\odot$).

S3.4 SN 2004gu

This slowly-declining SN from (Contreras et al. 2010), with a broad light curve ($x_1 = 1.37$, $s_{BV} = 1.19$) and photometric and spectroscopic similarities to SN 2006gz, has been mentioned in several papers about extreme “super-Chandra” SNe Ia (Yuan et al. 2010; Taubenberger et al. 2011; Silverman et al. 2011). A fit with SNOOPY suggests substantial host galaxy extinction ($E(B - V)_{\text{host}} = 0.18 \pm 0.02$ mag) with a fairly shallow extinction law ($R_{V,\text{host}} = 1.8 \pm 0.3$). The BOLOMASS reconstruction shows it to be super-Chandrasekhar-mass at $> 95\%$ confidence ($M_{\text{ej}} = 1.55^{+0.12}_{-0.08} M_\odot$, $M_{\text{Ni}} = 0.91^{+0.13}_{-0.12} M_\odot$), similar to SN 2005hj and the 1999aa-like SNF 20070506-006 (Scalzo et al. 2014a).

S3.5 SN 2005hj

Quimby, Höflich & Wheeler (2007) discussed this SN Ia in the context of its slow Si II $\lambda 6355$ velocity evolution near maximum light. They attribute this behavior to the presence of a dense shell in the outer layers of ejecta, a property of several non-homologous explosion models such as the tamped detonation and pulsating delayed detonation scenarios (Khokhlov, Mueller & Hoefflich 1993; Hoefflich & Khokhlov 1996). Similar slow evolution has also been observed in the super-Chandrasekhar-mass SN 2007if (Scalzo et al. 2010) and in several super-Chandrasekhar-mass candidates with 1991T-like spectra (Scalzo et al. 2012), and in fact occur frequently in 1991T-like SNe Ia (Benetti et al. 2005). Scalzo et al. (2012) argued that these explosions were tamped detonations resulting from prompt double-degenerate mergers exploding inside compact carbon-oxygen envelopes, and used v_{Si} to infer the contributions of these envelopes to the total ejected mass.

SN 2005hj itself is a slowly-declining ($x_1 = +1.43$, $s_{BV} = 1.19$), 1999aa-like (Quimby, Höflich & Wheeler 2007) SN Ia with modest reddening $E(B - V)_{\text{host}} = 0.12 \pm 0.02$ mag, $R_{V,\text{host}} = 1.4 \pm 0.5$. It reconstructs as super-Chandrasekhar-mass at $> 95\%$ confidence ($M_{\text{ej}} = 1.55^{+0.12}_{-0.08} M_\odot$, $M_{\text{Ni}} = 0.89^{+0.12}_{-0.11} M_\odot$), similar to SN 2004gu and the 1999aa-like SNF 20070506-006 (Scalzo et al. 2014a). Although the presence of a shell in the ejecta could affect the intrinsic color of the SN and hence the inferred reddening by host galaxy dust, M_{Ni} is not large enough to significantly affect our estimate of M_{ej} , as for SN 2005ls (see below).

S3.6 SN 2005ls

This CfA SN Ia from Hicken et al. (2009) is as slowly-declining ($x_1 = +0.83$, $s_{BV} = 1.24$) as spectroscopic 1991T-like SNe Ia, but its earliest spectrum was taken at day +8 (CBET 324), so its spectroscopic behavior before that point is unclear. It has a red color (SALT2 $c = +0.29$) and a large inferred $E(B - V)_{\text{host}} = 0.41 \pm 0.02$ mag ($R_{V,\text{host}} = 2.8 \pm 0.2$), so its inferred intrinsic color $(B - V)_{\max} = -0.12$ is blue but not extremely blue. Our inferred $A_V = 1.15 \pm 0.10$ mag is also consistent with the value obtained by Mandel, Narayan & Kirshner (2011) ($A_V = 0.81^{+0.93}_{-0.68}$ mag), though the latter infers lower $R_{V,\text{host}} = 2.1 \pm 0.2$.

Using the SNOOPY extinction values, SN 2005ls reconstructs as a luminous super-Chandrasekhar-mass candidate ($M_{\text{ej}} = 1.72^{+0.16}_{-0.12} M_\odot$, $M_{\text{Ni}} = 1.30^{+0.19}_{-0.17} M_\odot$). Using the looser BAYESN constraints on reddening, SN 2005ls remains luminous but is consistent with being Chandrasekhar-mass ($M_{\text{ej}} = 1.47^{+0.12}_{-0.09} M_\odot$, $M_{\text{Ni}} = 1.01^{+0.18}_{-0.17} M_\odot$).

This suggests that uncertainty in the extinction, and particularly in the extinction law slope, can in some cases drive systematic variations in our inference of M_{ej} ; the sampled models are ones with the minimum allowed fractions of intermediate-mass elements, so that adding ^{56}Ni requires a larger ejected mass. Although SN 2005ls formally passes our selection criteria, it has only one set of observations near B -band maximum light, with the next available observations at day +10; this may make the host galaxy extinction parameters more susceptible to systematic errors (e.g., in K -corrections within SNOOPY) than other SNe.

While SN 2005ls may thus be a good candidate for a super-Chandrasekhar-mass explosion, its status is dependent upon input assumptions to a greater extent than for other SNe Ia in this work. In other respects, SN 2005ls is generally consistent with the behavior of other 1991T-like SNe Ia in our sample that may be modestly, but not extremely, super-Chandrasekhar-mass.

S3.7 SN 2006bt

This SN Ia is described as peculiar by Foley et al. (2010) and Stritzinger et al. (2011): it is a Branch-CL event (with a cool photosphere near maximum light and Ti II $\lambda 4100$ features similar to SN 1991bg), but has a relatively broad light curve (SALT2 $x_1 = 0.07 \pm 0.10$) and a red apparent color (SALT2 $c = 0.16 \pm 0.01$). Foley et al. (2010) reports that the MLCS2k2 light curve fitter (Jha, Riess & Kirshner 2007) estimates $A_V = 0.43 \pm 0.05$ mag, even though the SN is far from the centre of an early-type galaxy, has non-standard color curves and shows no sign of Na I D absorption; they believe the actual extinction is negligible. Due to its photometric peculiarities, SN 2006bt is excluded from the training set for the SNOOPY color model of Burns et al. (2014). If applied anyway to the CfA light curve, SNOOPY gives $s_{BV} = 1.19$, $E(B - V)_{\text{host}} = 0.26 \pm 0.02$ mag, $R_{V,\text{host}} = 2.6 \pm 0.8$ mag, suggesting a highly extinguished event. Fitting the CSP-I light curve gives similar results.

We analyze the CfA light curve of SN 2006bt assuming no host galaxy reddening, although we still use $s_{BV} = 1.19$ to characterize the light curve and to evaluate the mean function for the GP interpolation. We find SN 2006bt is super-Chandrasekhar-mass at $> 95\%$ confidence, but with a moderate mass of ^{56}Ni ($M_{\text{ej}} = 1.62^{+0.23}_{-0.11} M_\odot$, $M_{\text{Ni}} = 0.48^{+0.08}_{-0.06} M_\odot$). This may be an underestimate of M_{ej} if SN 2006bt’s late-time NIR behavior is similar to SN 2006ot’s (see below), which seems likely given the similarity between their light curves where data are available (Stritzinger et al. 2011).

The CSP-I light curve for SN 2006bt does not formally pass our selection criteria, with the last optical-wavelength observations taken at day +39, and the last NIR observation at day +11; the coverage between that point and maximum is excellent. If we relax the requirements slightly, using the day +39 point as indicative of the late-time light curve behavior, and assume no host galaxy reddening, BOLOMASS predicts $M_{\text{ej}} = 1.82^{+0.37}_{-0.17} M_{\odot}$ and $M_{\text{Ni}} = 0.48^{+0.08}_{-0.06} M_{\odot}$, consistent with the estimate from the CfA light curve.

In contrast to SN 2005ls or other highly reddened events, SN 2006bt's modest value of M_{Ni} makes its inferred value of M_{ej} more robust to systematic errors in reddening or distance. A cross-check using a loose Gaussian prior $E(B - V)_{\text{host}} = 0.1 \pm 0.1$ mag, $R_{V,\text{host}} = 3.1 \pm 1.0$ suggests that $M_{\text{ej}} > 1.5 M_{\odot}$ (99% confidence) for a range of plausible values of $E(B - V)_{\text{host}}$ and $R_{V,\text{host}}$.

It thus seems likely either that SN 2006bt is super-Chandrasekhar-mass, with $M_{\text{ej}} \sim 1.7 M_{\odot}$, or that it somehow violates one or more of our modeling assumptions (such as stratified ejecta or a standard density profile) without showing dramatic spectroscopic peculiarities. In either case, typical Chandrasekhar-mass models are probably not well-suited to describe the physics of the explosion.

S3.8 SN 2006gt

This SN Ia is one of two Branch-CL events for which SNID finds a 1991bg-like spectroscopic subtype. It is a fast-declining event ($x_1 = -1.81$, $s_{BV} = 0.53$) with a red color $(B - V)_{\text{max}} = 0.05$ mag after correction for mean extinction. SNOOPY estimates of the host galaxy extinction using the CSP-I and CfA light curves are mutually consistent: $E(B - V)_{\text{host}} = 0.06 \pm 0.02$ mag (CfA: 0.08 ± 0.04 mag), $R_{V,\text{host}} = 2.7 \pm 1.0$ (CfA: 3.3 ± 1.3). We use the CSP-I light curve to reconstruct it as a sub-Chandrasekhar-mass event ($M_{\text{ej}} = 0.86^{+0.05}_{-0.03} M_{\odot}$, $M_{\text{Ni}} = 0.27^{+0.04}_{-0.04} M_{\odot}$).

S3.9 SN 2006gz

This peculiar SN Ia from Hicken et al. (2007) is one of the exemplars of the extremely luminous ‘‘super-Chandra’’ events with unusually slowly-declining light curves (see also Howell et al. 2006; Scalzo et al. 2010; Yuan et al. 2010; Silverman et al. 2011; Taubenberger et al. 2011). However, discussion of the super-Chandrasekhar-mass nature of this event has hinged mostly on inferences about M_{Ni} , which has been called into question (Maeda et al. 2009; Maeda & Iwamoto 2009; Scalzo et al. 2010). Hicken et al. (2007) also cite evidence for C II absorption at early phases, although such features are now believed to be present in 20%–30% of normal SNe Ia (Thomas et al. 2011; Parrent et al. 2011; Folatelli et al. 2012). Taubenberger et al. (2013) argue that the nebular spectra of SN 2006gz are more similar to the super-Chandra SNe Ia 2007if and 2009dc than to 1991T-like SNe Ia, which presumably can be explained as near-Chandrasekhar-mass explosions.

A fit with SALT2 yields $x_1 = 2.18 \pm 0.12$, $c = 0.11 \pm 0.03$, while a SNOOPY fit suggests $s_{BV} = 1.31$, the largest value in our sample. The host galaxy extinction parameters according to SNOOPY are $E(B - V)_{\text{host}} = 0.17 \pm 0.02$ mag and $R_{V,\text{host}} = 4.1 \pm 1.9$, consistent with the values assumed by Hicken et al. (2007). Under these assumptions, we infer $M_{\text{Ni}} = 1.34^{+0.31}_{-0.28} M_{\odot}$, again consistent with Hicken et al. (2007), and $M_{\text{ej}} = 2.05^{+0.28}_{-0.19} M_{\odot}$, comparable to the value inferred for SN 2007if using similar methods (Scalzo et al. 2010).

Given the danger that overcorrection for host galaxy reddening may bias M_{Ni} , and hence M_{ej} , we run a separate reconstruction assuming zero host galaxy extinction. This run yields $M_{\text{ej}} = 1.93^{+0.41}_{-0.17} M_{\odot}$, $M_{\text{Ni}} = 0.64^{+0.11}_{-0.09} M_{\odot}$, so that the super-Chandrasekhar-mass nature of SN 2006gz is secure irrespective of the ^{56}Ni content. We can place a firm 99% confidence lower limit $M_{\text{ej}} > 1.6 M_{\odot}$ on the ejecta even with the most conservative assumptions about reddening.

S3.10 SN 2006ot

Stritzinger et al. (2011) note the photometric peculiarity of SN 2006ot as well as its similarity to SN 2006bt, although spectroscopically it is a Branch-BL SN Ia with the highest at-maximum Si II velocity in our sample (13989 km s^{-1} ; Folatelli et al. 2013). As with SN 2006bt above, SN 2006ot was excluded from the training set for the SNOOPY color model of Burns et al. (2014), and Stritzinger et al. (2011) find both objects suffered little to no host galaxy extinction.

SN 2006ot does not pass our full selection criteria, with the first optical-wavelength data appearing at day +3 after B -band maximum. However, it has well-sampled coverage in CSP-I $BVgrYJ$ past day +40 and CSP-I u out to day +35, so despite some uncertainty on the maximum-light bolometric luminosity, our reliance on templates to fill in regions of missing observations is minimal. This is fortunate, since we find that $\Delta m_{40,\text{bol}}$ is overestimated by 0.1 mag if we use the SNOOPY predictions for the YJH light curves instead of the GP interpolation model. Given that SN 2006bt does not have late-time u or NIR data, we can be reasonably certain that we have underestimated its mass somewhat by using template corrections for this missing flux near day +40.

As in the case of SN 2006bt, we analyze SN 2006ot assuming negligible host galaxy extinction ($E(B - V)_{\text{host}} = 0.00 \pm 0.05$ mag). We propagate an uncertainty of ± 3 days on the date of B -band maximum into the rise time, and adjust the maximum-light bolometric luminosity upwards by 10% to reflect the decline by day +3. The resulting BOLOMASS run shows that SN 2006ot is super-Chandrasekhar-mass at high confidence ($M_{\text{ej}} = 1.91^{+0.43}_{-0.20} M_{\odot}$, $M_{\text{Ni}} = 0.50^{+0.09}_{-0.07} M_{\odot}$). A separate analysis with loose Gaussian priors $E(B - V)_{\text{host}} = 0.1 \pm 0.1$ mag and $R_{V,\text{host}} = 3.1 \pm 1.0$ places a firm 99% confidence level lower limit of $1.6 M_{\odot}$ on M_{ej} given any plausible value for $E(B - V)_{\text{host}}$. This lower limit is conservative, in the sense that all adjustments made above tend to reduce the inferred value of M_{ej} .

S3.11 SN 2007ba

This SN Ia is the other spectroscopic 1991bg-like in our sample. Like SN 2006gt, it is also a fast-declining event ($x_1 = -1.64$, $s_{BV} = 0.59$) with a red color $(B - V)_{\text{max}} = 0.05$ mag after correction for mean extinction. SNOOPY estimates of the host galaxy extinction using the CSP-I and CfA light curves are marginally consistent: $E(B - V)_{\text{host}} = 0.23 \pm 0.02$ mag (CfA: 0.16 ± 0.04 mag), $R_{V,\text{host}} = 1.7 \pm 0.3$ (CfA: 1.8 ± 0.9). Using the CSP-I light curve, we infer a sub-Chandrasekhar mass for SN 2007ba at $> 95\%$ confidence ($M_{\text{ej}} = 1.11^{+0.09}_{-0.07} M_{\odot}$, $M_{\text{Ni}} = 0.48^{+0.08}_{-0.07} M_{\odot}$).

The high mass, relative to other Branch-CL events with similar light curve shapes, is intriguing, and worth investigating for systematic errors. SN 2007ba has its last u -band measurement at day +22, although this should be late enough for the u -band color to have stabilized and for later measurements to be reasonably well-predicted by SNOOPY. SN 2007ba also has excellent NIR coverage, with YJH measurements extending out to day +48.

With a maximum *a posteriori* probability of $P_{\text{fit}} = 0.004$, the BOLOMASS model fit is not particularly good, further suggesting SN 2007ba is unique among the objects considered in our study. Inspection of the light curve fit shows that the radioactive deposition curve agrees well with the observed bolometric light curve at days +44 and +46, but underpredicts day +55 by almost 25%. The *B*-band light curve falls below magnitude 21.0 near day +40 and begins to *brighten* after day +45, suggesting that measurements at such faint magnitudes may not be reliable despite larger reported uncertainties. If we remove the day +55 measurement from the fit and run BOLOMASS again, we get nearly the same results ($M_{\text{ej}} = 1.09^{+0.07}_{-0.06} M_{\odot}$, $M_{\text{Ni}} = 0.48^{+0.08}_{-0.07} M_{\odot}$) with a much better fit ($P_{\text{fit}} = 0.338$). We also get the same results if we allow points as early as day +30 into the fit, arguing that less massive ejecta should enter the Compton-thin regime (assumed by BOLOMASS) earlier than most SNe Ia.